# Development of a Modular MDO Framework for Preliminary Wing Design

by

Ricardo Miguel Paiva
BSc - Instituto Superior Tecnico, PORTUGAL, 2005

A Thesis Submitted in Partial Fulfillment of the
Requirements for the Degree of
MASTER OF APPLIED SCIENCE
in the
Department of Mechanical Engineering.



University of Victoria

# Supervisory Committee

Dr. Afzal Suleman, Supervisor (Department of Mechanical Engineering, University of Victoria)

Dr. Curran Crawford, Supervisor (Department of Mechanical Engineering, University of Victoria)

Dr. Zuomin Dong, Departmental Member (Department of Mechanical Engineering, University of Victoria)

Dr. Lin Cai, External Member (Department of Electrical and Computer Engineering, University of Victoria)

**Supervisory Committee:**

Dr. Afzal Suleman, Supervisor
(Department of Mechanical Engineering, University of Victoria)

Dr. Curran Crawford, Supervisor
(Department of Mechanical Engineering, University of Victoria)

Dr. Zuomin Dong, Departmental Member
(Department of Mechanical Engineering, University of Victoria)

Dr. Lin Cai, External Member
(Department of Electrical and Computer Engineering, University of Victoria)

# Abstract

Multidisciplinary Design Optimization (MDO) is an area in engineering design which has been growing rapidly in terms of applications in the last few decades, aircraft design being no exception to that. The application of MDO to aircraft and more specifically, wing design, presents many challenges, since disciplines like aerodynamics and structures have to be combined and interact. The level to which this interaction is implemented depends only on how much one is willing to pay in terms of computational cost.

The objective of the current work is therefore to develop a simplified MDO tool, suitable for the preliminary design of aircraft wings. At the same time, versatility in the definition of optimization problems (in terms of design variables, constraints and objective function) is given great attention. At the same time, modularity will ensure that this framework is upgradeable with higher-fidelity and/or more capable modules.

The disciplines that were chosen for interaction were aerodynamics and structures/aeroelasticity, though more data can be extracted from their results in order to perform other types of analyses. The aerodynamics module employs a Vortex Lattice code developed specifically for the current implementation of the tool. The structural module is based on Equivalent Plate model theory. The fluid structure interaction is simply one-way, wherein the aerodynamics loads are passed on to the structural analyzer for computation of the static deformation. Semi-empirical relations are then used to estimate the flutter speed. The optimizer, which controls the activity of the other modules, makes use of a gradient based algorithm (Sequential Quadratic Programming) to search for a local minimum of a user defined objective function.

Among the myriad of MDO strategies available, two are chosen to exemplify the modularity of the tool developed: Multidiscipline Feasible (MDF) and Sequential Optimization (SO), and their results are compared. Several case studies are analyzed to cover a broad spectrum of the capabilities of the framework.

Because user interaction is of prime concern in design optimization, a graphical interface (GUI) of the tool is presented. Its advantages in terms of the set up of optimization problems and post-processing of results are made clear.

In conclusion, some topics for future work regarding the expansion and improvement of the features of the application are noted.

# Contents

# List of Figures

# List of Tables

# Nomenclature

| | |
|---|---|
| $a$ | Local speed of sound [m.s$^{-1}$] |
| $A$ | Aspect Ratio |
| $\mathbf{A}$ | Inequality linear constraints coefficient matrix |
| $\mathbf{A_{equality}}$ | Equality linear constraints coefficient matrix |
| $\mathbf{b}$ | Linear constraints RHS vector |
| $\mathbf{b_{equality}}$ | Equality linear constraints RHS vector |
| $bs$ | Spanwise location of the breakstation [m] |
| $\frac{b}{2}$ | Semispan [m] |
| $\mathbf{c}$ | Nonlinear constraints vector |
| $\mathbf{c_{equality}}$ | Equality nonlinear constraints vector |
| $c_{bs}$ | Chord at breakstation [m] |
| $C_D$ | Coefficient of drag |
| $C_{D_f}$ | Coefficient of drag at zero lift (friction and form drag) |
| $C_f$ | Coefficient of friction |
| $C_{D_i}$ | Coefficient of lift induced drag |
| $C_{D_{wave}}$ | Coefficient of wave drag |
| $C_l$ | Sectional lift coefficient (2D) |
| $C_L$ | Lift coefficient (3D) |
| $C_{l_{max}}$ | Maximum coefficient of lift of the airfoil |
| $C_{L_{max}}$ | Maximum coefficient of lift of the wing |
| $C_{L_\alpha}$ | Derivative of the coefficient of lift (3D) with respect to the angle of attack |
| $C_M$ | Pitching moment coefficient |
| $C_{M_\alpha}$ | Derivative of the pitching moment coefficient with respect to the angle of attack |
| $C_{mn}$ | Vortex lattice influence coefficients |

| | |
|---|---|
| $c_r$ | Chord at root [m] |
| $c_t$ | Chord at tip [m] |
| $D$ | Total drag force [N] |
| $D_{ij}$ | Constitutive matrix [N.m$^{-2}$] |
| $E$ | Young's Modulus [N.m$^{-2}$] |
| $FF$ | Form factor |
| $G$ | Shear Modulus [N.m$^{-2}$] |
| $K_{ij}$ | Equivalent plate stiffness matrix |
| $\ell$ | Vortex filament length [m] |
| $L$ | Total lift force [N] |
| **LB** | Design variables lower bounds vector |
| $m_{wing}$ | Wing mass [Kg] |
| $M_{crit}$ | Critical Mach number |
| $M_{eff}$ | Effective Mach number |
| $M_{ij}$ | Equivalent plate mass matrix |
| $M_\infty$ | Freestream Mach number |
| $\mathbf{n}$ | Surface normal |
| $\mathbf{P}\,(x, y, t)$ | Applied loads field [N.m$^{-2}$] |
| $Pr$ | Prandtl number |
| $Q$ | Work done by external forces [J] |
| $r$ | Recovery factor |
| $r_\alpha$ | Non dimensional radius of gyration of the wing |
| $Re$ | Reynolds number |
| $S_{ref}$ | Reference surface area |
| $S_{wet}$ | Wetted surface area |
| $u$, $v$, $w$ | Equivalent plate displacement field [m] |
| $u_0$, $v_0$, $w_0$ | Equivalent plate initial displacement field [m] |
| $u_{ind}$, $v_{ind}$, $w_{ind}$ | Induced velocity field [m.s$^{-1}$] |
| $\mathbf{V}_{ind}$ | Total induced velocity [m.s$^{-1}$] |
| $T$ | Total kinetic energy [J] |
| $U$ | Total internal energy [J] |
| **UB** | Design variables upper bounds vector |
| $V_d$ | Divergence speed [m.s$^{-1}$] |

| | |
|---|---|
| $V_f$ | Flutter speed [m.s$^{-1}$] |
| $V_\infty$ | Freestream velocity [m.s$^{-1}$] |
| $W$ | Wing weight [N] |

# Greek Symbols

| | |
|---|---|
| $\alpha$ | Angle of attack [rad] or [deg] |
| $\beta$ | Prandtl-Glauert correction factor |
| $\gamma$ | Specific heat ratio |
| $\Gamma$ | Vortex circulation $[m^2.s^{-2}]$ |
| $\delta_{tip}$ | wing tip displacement [m] |
| $\epsilon$ | Non dimensional distance from a wing section center of mass to the aerodynamic center |
| $\epsilon_i$ | Strain tensor |
| $\Lambda_{LE}$ | Leading edge sweep angle [rad] or [deg] |
| $\Lambda_{0.25c}$ | 25% chordline sweep angle [rad] or [deg] |
| $\nu$ | Poisson ratio |
| $\rho$ | Air density [Kg.m$^{-3}$] |
| $\sigma_{ij}$ | Stress tensor [N.m$^{-2}$] |
| $\phi_x$, $\phi_y$ | Rotation fields |
| $\varphi$ | Dihedral angle [rad] or [deg] |
| $\omega_\alpha$ | First uncoupled torsional frequency [rad.s$^{-1}$] |
| $\omega_i$ | i-th natural vibration frequency [rad.s$^{-1}$] |

# Acronynms

| | |
|---|---|
| AOA | Angle Of Attack |
| BWB | Blended Wing Body |
| CFD | Computational Fluid Dynamics |
| CO | Collaborative Optimization |
| CPT | Classical Plate Theory |
| DV | Design Variable |
| EPM | Equivalent Plate Model |
| FEM | Finite Element Model(s) |

| | |
|---|---|
| FSDT | First-order Shear Deformation Theory |
| GUI | Graphical User Interface |
| LE | Leading Edge |
| MAC | Mean Aerodynamic Chord |
| MDF | Multidiscipline Feasible |
| NACA | National Advisory Committee for Aeronautics |
| SO | Sequential Optimization |
| SQP | Sequential Quadratic Programming |
| TE | Trailing Edge |
| VLM | Vortex Lattice Method |

# Acknowledgements

First and foremost I would like to acknowledge my supervisors, Dr. Afzal Suleman and Dr. Curran Crawford for their support and, most of all, for sharing their expertise in this field.

My thanks also go to my friends in Canada and in Portugal. I would like to express my gratitude to my good friend Andre Carvalho who was never hesitant to share his programming expertise. To Kerem Karakoc, Casey Keulen, and Jenner Richards for the time well spent at our office. To Bruno and Joana Rocha, who together with Helena form the nicest family I know. To Carlos Silva for his opportune tips on optimization. Also, to Ali Taleb and the UVic AERO team for their friendship. A special thanks to Sandra Makosinski for her dedication to the welfare of our research group.

Last but not least, I would like to thank my family, specially my parents who were always supportive although miles away.

*To my family...*

# Chapter 1

# Introduction

## 1.1 Background

### 1.1.1 Multidisciplinary Optimization

The main reason behind design optimization in engineering in general, and aerospace engineering in particular, is to bring about the ability to realize a design's full potential, by balancing conflicting requirements in a harmonious fashion. The benefits are twofold: older designs can be optimized in order to keep competitiveness, while newer, usually immature, designs, can be realized closer to their full potential, from the moment of inception. This helps in clearing whatever obstacles the introduction of a new technology might present.

Typically, in aerospace applications, synergy is required between different disciplines such as aerodynamics, structures, aeroelasticity and cost, to name a few. Though these are the most common, almost every aspect of aircraft design may be introduced into the optimization process, such as environmental performance (Antoine and Kroo [1], [2]), which has become a growing concern over the last few years

given increasingly stringent regulations. The concept of Multidisciplinary Design Optimization (MDO) arises from this need to incorporate such different types of analyses. Beyond dwelling into numerical optimization techniques, MDO also involves the efficient combination of the different disciplines in a way that minimizes computational cost and increases the chances of finding a design point that brings significant improvement.

The past 30 years have been prolific for the MDO area, mainly due to the compounding power of digital computers. General approaches to MDO, in an attempt to unify the various strategies, were the object of various papers: [3], [4], [5].

Rather than the other way around, MDO has actually expedited or led to the development of new, advanced optimization techniques, such as the adjoint method and its numerous derivations ([6], [7], just to cite a few) and Distributed optimization (clinging at the borders of Artificial Intelligence with Probability Collectives [8]).

An example of previous work on an MDO framework is the Bi-Level Integrated System Synthesis (BLISS)-based application, developed by Sobieski et al. [9], [10], using a Collaborative Optimization (CO) implementation in MATLAB® and iSIGHT®. Other MDO tools worthy of mention are Wakayama's *WingMOD* [11], specialized for the optimization of Blended Wing Body (BWB) aircraft, and the application developed by Ko also intended for BWB optimization but with provisions for a Distributed Propulsion concept [12]. *WingOpt* [13] is another example, one that actually uses the same type of solvers as the MDO tool developed in this thesis. Standalone, deployable MDO applications are, however, scarce.

Another area of concern in MDO is the fact that for increasingly complex problems, the problem set up itself, as well as the post processing, can become too cumbersome for the regular user. Therefore, the introduction of a Graphical User Interface (GUI) is always welcome. An example of the use of off-the-shelf CAD tools for visu-

alization of the design optimization process is presented in [14]. Another interesting approach in the use of graphical interfaces in optimization tools is the real-time constraint visualization implemented by Deremaux [15].

Lastly, the modular nature of an MDO framework ensures that it is adaptable to other types of problems in aerospace optimization (and, with additional effort to other engineering design problems). More importantly, it allows the analyzer modules to be updated in order to increase the level of fidelity of the analyses they produce. The same holds true of course for the optimizer module(s). An example of an MDO implementation capable of using two levels of fidelity for the analyses is detailed in [16].

### 1.1.2 Aircraft wing design

Wing design is a critical stage in aircraft development, as it determines most of the performance and flight qualities of the final aircraft. It is also the component that sustains the greatest loads as it is providing the required lift for flight. Hence it is the main focus in the scope of the current work.

Though wing geometry and construction underwent a series of changes throughout the history of aircraft, it has been a long time since the planform for commercial airliners has undergone significant changes. The general shape proposed by Boeing in the 1950's in the form of the B707 (see Figure 1.1) has served as a baseline for almost every subsonic airliner design since (an example is the Airbus A380, represented in Figure 1.2).

This is partially due to the high costs involved in developing new, unproven, designs, rather than relying on what one knows that works. On the other hand, this configuration may already be close to the optimum, given the flight conditions and

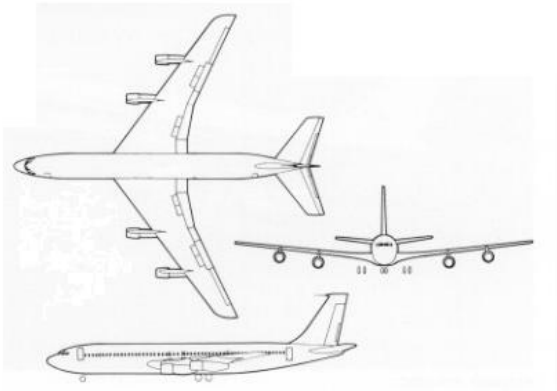

Figure 1.1: Boeing 707

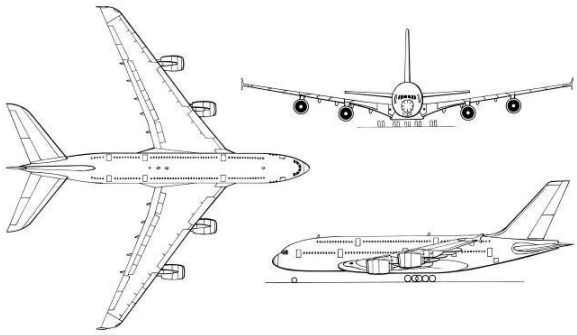

Figure 1.2: Airbus A380

constraints it was designed for. Therefore, improving upon such a design may be challenging, given the low sensitivities observed around this design point.

In terms of wing internal structure, the evolution has been mostly in terms of material technology and fabrication techniques. The major evolution in this field probably came with the introduction of composite materials. The conventional wing structure design with spars, ribs, stringers and skin, dates back to the times of World War II and is still widely used (and exemplified in Fig. 1.3). Recent advances in smart structures have led to radically different structural arrangements, such as aeroelasti-

cally tailored and morphing wings. These are, however, still research topics that have yet to see widespread use in the world of aviation.

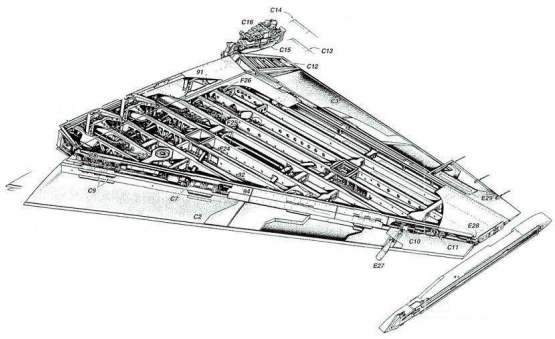

Figure 1.3: F-16 wing structure

## 1.2 Thesis Objective

One of the main deficiencies of most MDO tools developed thus far is that they lack the versatility to adapt to a wide array of scenarios and are usually bound to solving for a predetermined set of design variables. The main objective of this work is therefore to create an MDO tool where modularity, ease of use and relatively low computational cost combine harmoniously. To that end, the fidelity of each of the modules that comprise such a tool (analyzer modules and optimizer, as we shall see) is somewhat reduced, since more development time was devoted to creating a docking point for all of them.

It is also understood that while the interface of the tool itself should remain as general as possible, the modules are to be limited to analyzing a fraction of the flight

envelope (aerodynamics) and only consider conventional wing construction (structures), in order to keep development phase within a reasonable time frame. To that end, the subsonic regime was chosen for the aerodynamics analysis, as fast and proven methods for the prediction of aerodynamic loads for air speeds fall within this range. With such limitations in mind, the tool is primarily intended for the design of commercial aircraft wings, from airliners to small business jets and utility aircraft. It is also to these that the case studies presented in Chapter 5 are dedicated to.

## 1.3 Thesis Outline

This thesis is divided into six chapters.

In Chapter 2, the aerodynamics modeling of the wing is defined and most aerodynamic and geometric variables of interest are introduced. The aerodynamic performance is estimated through a computational application based on the Vortex Lattice Method (VLM) and a semi-empirical boundary layer calculation. The module developed, called *Zephyr*, is then benchmarked against cases found in the literature and other VLM codes.

Chapter 3 details the development of the structural/aeroelasticity module. The module employs a third party program, *Awing*, based on Equivalent Plate Model theory. This allows the determination of both static deformation under the aerodynamic loads computed in the aerodynamics module and computation of the eigen modes of the wing structure. A validation case is also presented. As an add-on to this module, semi-empirical expressions that allow the determination of aeroelastic instabilities are introduced.

The objective of Chapter 4 is to give an overview of the capabilities of the tool developed and its graphical user interface (GUI), which is believed to increase its

productivity significantly, especially in terms of post-processing.

In Chapter 5, the wing design optimization problem is posed, emphasizing the versatility of the tool in terms of the customization of the set of design variables (DV's), constraints and objective function. Several case studies are considered in order to showcase the capabilities of the tool. These comprise single and multi-objective optimization, standalone disciplinary analysis and also two different MDO strategies that were implemented in the code (Multi-Discipline Feasible and Sequential Optimization).

Finally, in Chapter 6, conclusions are drawn from the results presented and the satisfactory fulfillment of the objectives is discussed. Additionally, some suggestions are hinted at on how to improve the MDO framework developed, as basis for future work.

## 1.4 Coordinate system

The reference coordinate system attached to the wing and used throughout the course of this work is sketched in Figure 1.4. The origin is located at the leading edge of the root chord, which is aligned with the $x$-axis.

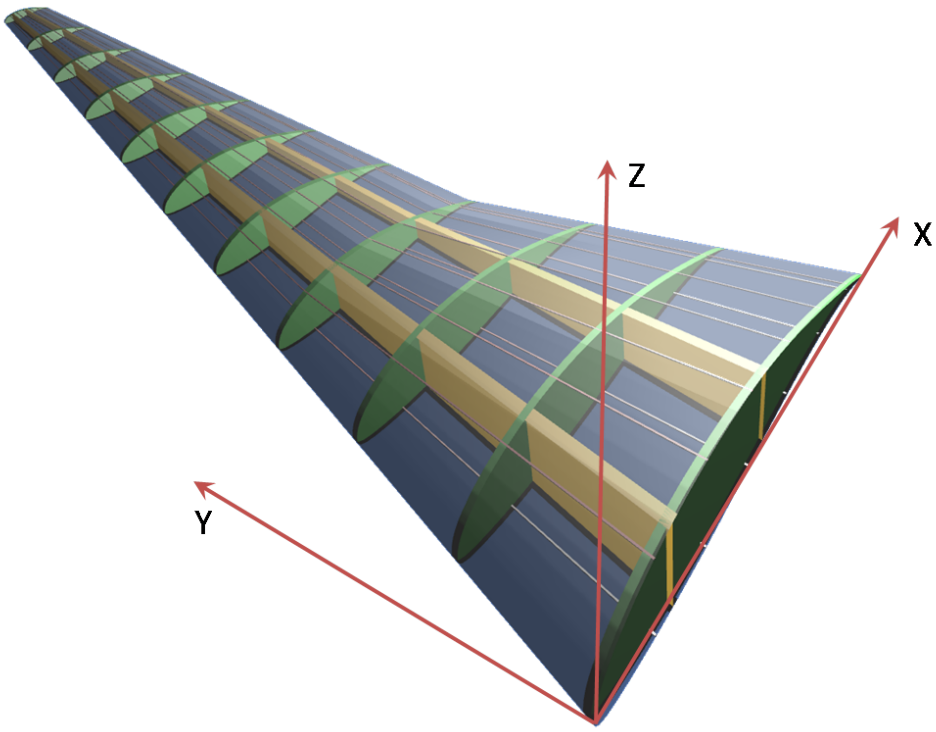


Figure 1.4: Coordinate system for wing geometry

# Chapter 2

# Aerodynamics Solver

As mentioned in the previous chapter, a fast aerodynamics solver is required. We are interested in characterizing a three dimensional wing in a way that the load distribution across the planform is solved for (for subsequent use in the structural module). Simple empirical formulas for the evaluation of non-dimensional coefficients would not provide sufficient accuracy or resolution since the final output required is the load distribution on a three dimensional wing. The remaining option is to employ CFD techniques to compute the flow around the wing up to the high subsonic regime.

## 2.1 The Vortex Lattice Method

Computational cost and simplicity are a major concern since, after all, each of the modules may be required to perform hundreds of evaluations depending on the number of design variables taken into consideration during optimization. Also, a computationally costly finite difference/volume approach to either the Euler or Navier Stokes equations for fluid flow in three dimensions is undesirable. Instead, the Vortex

Lattice Method (VLM) has been employed, as it is relatively simple to implement, the price paid in terms of fidelity of the model is more than outweighed in terms of its versatility, and there are significant savings in solution time. It was formulated as early as the 1930's though, like many others, it did not see widespread use until digital computers were introduced. It shares most of its limitations with panel methods. Along with these, the VLM is part of a family of techniques which employ the incompressible, inviscid and irrotational form of the Navier Stokes equations, simplifying to the Laplace equation for potential flow. Solving the Laplace equation is a reasonable alternative that provides adequate results for moderate angles of attack and streamlined geometries. According to Margason et al. [17]:

> The VLM predicts the experimental data very well, due to the fact that vortex lattice methods neglect both thickness and viscosity effects. For most cases, the effect of viscosity offsets the effect of thickness, fortuitously yielding good agreement between the VLM and experiment.

These methods, though more than adequate to describe low-speed, subsonic flows about aircraft wings, require some corrections for high-speed subsonic flow due to compressibility effects. A separate estimation of skin friction drag is also required.

### 2.1.1 Theory

The derivation of the theory behind the vortex lattice method presented here follows [18], [19], [20] and [21] very closely. Toward the end, some simplifications are dropped in favor of a more complex, yet still computationally efficient model. These simplifications were originally introduced as many VLM codes were developed at a time when the processing prowess of regular desktop computers was several orders of

magnitude below what it is today. One of the first assumptions to be made is that the geometry is assumed to be symmetric - only the right wing is represented.

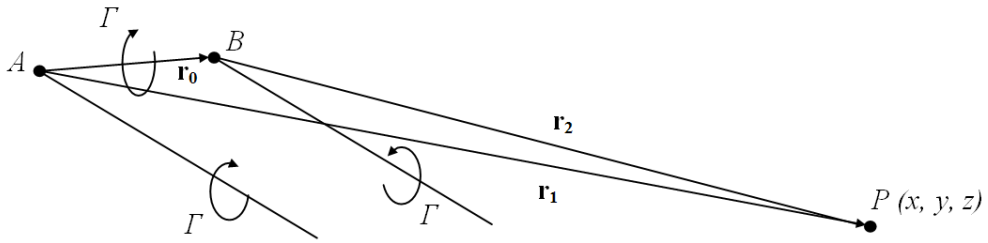


Figure 2.1: The horseshoe vortex element

We start by defining the horseshoe vortex (see Figure 2.1), which is basically composed of a finite vortex filament coupled with two semi-infinite filaments. Many other formulations for the horseshoe vortex exist, although only the classical one is presented here. A complete derivation of the mathematics of the horseshoe element is present in Appendix A. From this derivation, we obtain the velocity imparted at an arbitrary control point by a single horseshoe vortex (Eqs. (A.15), (A.16), (A.17), (A.18), (A.19)). In order to build a vortex lattice, however, an array of these vortices must be placed on the wing. This yields the following expression for the velocity induced at the $m^{th}$ control point by all the $2N$ other vortices (each of them denoted by the index $n$):

$$\mathbf{V}_{m_{ind}} = u_{m_{ind}}\mathbf{i} + v_{m_{ind}}\mathbf{j} + w_{m_{ind}}\mathbf{k} = \sum_{n=1}^{2N} \mathbf{C}_{mn}\Gamma_n \tag{2.1}$$

The influence coefficients can be readily extracted from the result of the derivation in Appendix A. They depend solely on the geometry and therefore, if we knew the strength of the vortices, we could compute the induced velocities.

One of the major differences between the VLM and panel methods is that in the former the singularities are placed on the mean surface of the wing, rather than on the actual surface. This distribution of vorticity seeks to emulate the changes in velocity induced on the flow as it traverses the upper and lower surfaces of a wing. The actual laying down of the vortices on the mean surface is seldom used (though the code that was developed supports that feature, as we shall see further ahead). Even for cambered airfoils, a simple planar surface is usually enough to obtain good results [19]. This surface is then divided into elemental panels where the spanwise vortex ($AB$) is bound to the line at quarter chord of the panel. The control point is placed midspan of each panel, at three quarter panel chord. In the present case there is a need for multiple spanwise and chordwise elements so as to better characterize the load distribution.

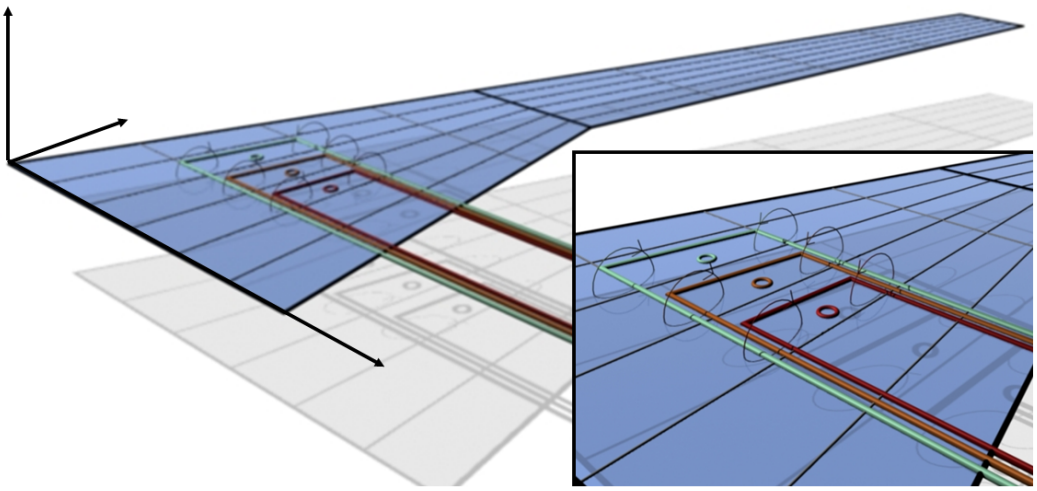

Figure 2.2: Vortex lattice

The boundary condition for the velocity is such that the flow never crosses the mean surface, i.e., an impermeability condition. Therefore, summing the freestream

velocity with the induced velocity should yield, at each control point:

$$\mathbf{V} \cdot \mathbf{n} = 0 \tag{2.2}$$

If the surface is defined explicitly as $z = f(x, y)$, then the surface normal:

$$\mathbf{n} = \left( -\frac{\partial f}{\partial x}, -\frac{\partial f}{\partial y}, 1 \right) \tag{2.3}$$

which combined with the definition of the freestream velocity:

$$\mathbf{V}_\infty = V_\infty \cos\alpha \, \mathbf{i} + V_\infty \sin\alpha \, \mathbf{j} \tag{2.4}$$

gives:

$$\sum_{n=1}^{2N} \left[ C_{mn_\mathbf{k}} - C_{mn_\mathbf{i}} \frac{\partial f}{\partial x} - C_{mn_\mathbf{j}} \frac{\partial f}{\partial y} \right] \Gamma_n = V_\infty \left( \cos\alpha \frac{\partial f}{\partial x} - \sin\alpha \right) \tag{2.5}$$

Because symmetry is invoked (the distribution of circulation, $\Gamma$, is symmetric), the system only has $N$ equations rather than $2N$. The influence coefficients of the opposite side are calculated at the same time as those for the $n^{th}$ horseshoe, so that:

$$C_{mn_{\mathbf{i},\mathbf{j},\mathbf{k}}} = C_{mn_{\mathbf{i},\mathbf{j},\mathbf{k}\ left}} + C_{mn_{\mathbf{i},\mathbf{j},\mathbf{k}\ right}} \tag{2.6}$$

where $C_{mn_{\mathbf{i},\mathbf{j},\mathbf{k}}}$ means the procedure is repeated individually for each of the three directions.

Vortex line extensions have to be handled carefully as they may go through (or pass very close to) control points, effectively making the equations singular. When this happens, those coefficients may be set to zero (otherwise the induced velocity would tend to infinity in the vicinity of the vortex core). Upon solving the system of equations and obtaining each panel's vortex strength, the circulations on the trailing

vortices should be updated since they are superimposed along a chordline. Afterwards, the computation of lifting and induced drag forces may take place by using the Kutta-Joukowski theorem (for each panel):

$$\mathbf{F} = \rho \mathbf{V} \times \Gamma \ell \tag{2.7}$$

where $\ell$ is a vector that represents the bound vortex filament on each elemental panel. These forces, once calculated, may be decomposed into the wind axes thus originating the lift and induced drag forces. Another way to estimate these forces would be to do a Trefftz plane analysis, where induced velocities are evaluated at the wake, at some distance downstream of the wing [20]. Such a procedure should be more accurate, especially when the bending of the wake is modeled. The downside is, of course, added complexity to the code.

In order to assemble the system of equations, the actual definition of the surface where the vortices lie is required. This is the main topic of the next section.

### 2.1.2 Geometric design variables and panel layup

A specific wing planform, driven by a restricted set of design variables, has been chosen to define the design space, as shown in Figure 2.3. This approach provides coverage of a wide trade space, while remaining tractable. It is believed that this description is sufficient for subsonic aircraft wings.

At this point, it is not yet clear how to compute points across the mean surface in order to both lay down the mesh (if the conformal option is chosen) and estimate the derivatives in Eq. (2.5) through finite differencing. The answer comes from nondimensionalized arrays of points (sorted according to the order set in Figure 2.4) describing each of the three airfoils that forms the wing. These can be stored into

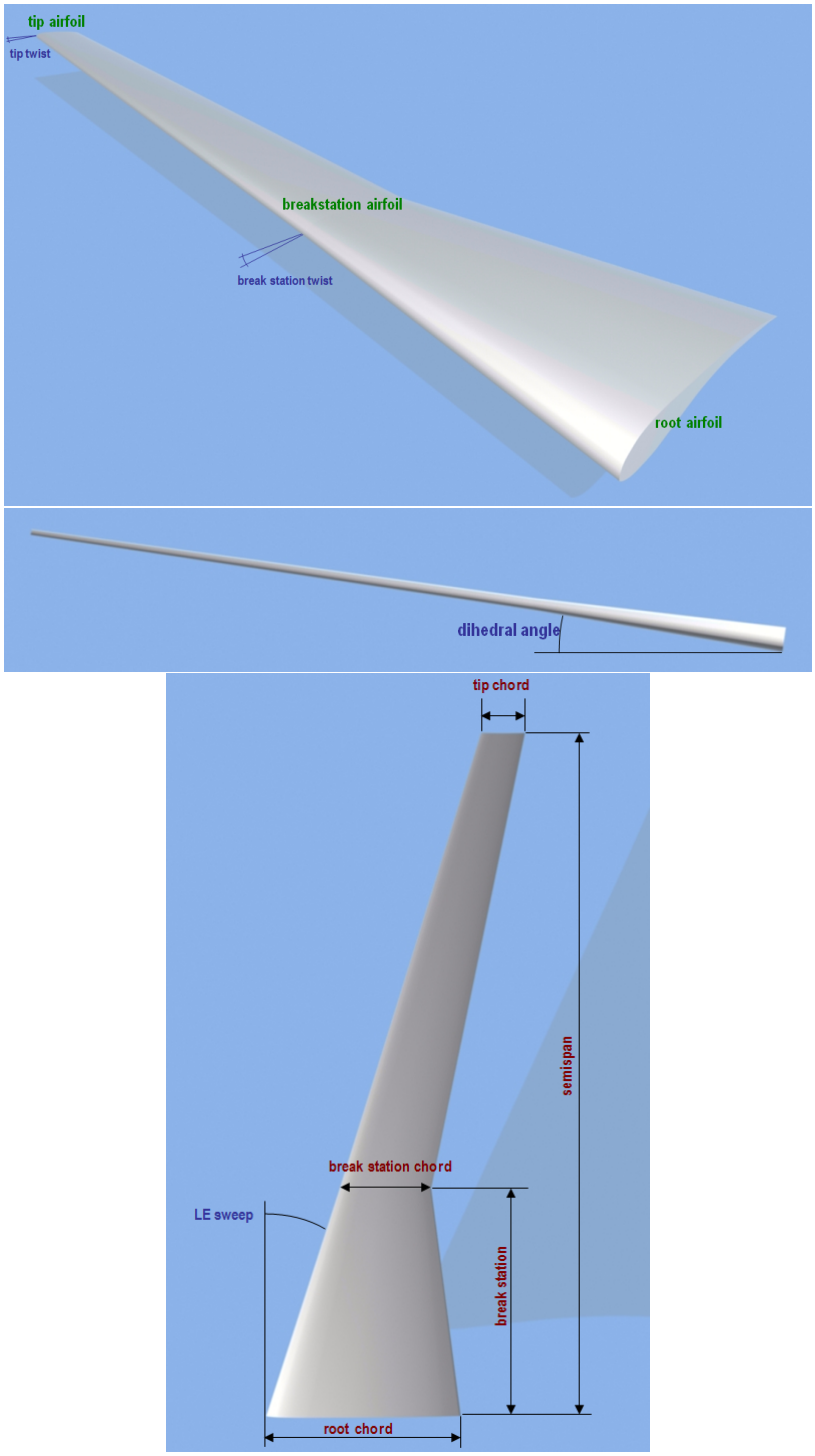


Figure 2.3: Geometry design variables

files and are easily obtainable from online databases [22]. The camberline (the line

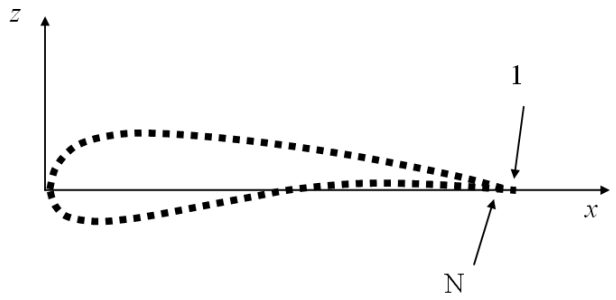


Figure 2.4: Sorting airfoil data

that rests exactly halfway between the upper and lower surfaces) of these airfoils is then interpolated by means of cubic splines. It is then a matter of linearly extruding these three lines in order to create two different surfaces. In general, this is bound to cause a discontinuity in the $y$-derivative at the breakstation, though that never poses as a problem since no control point - which is where the derivatives are computed - ever lies there.

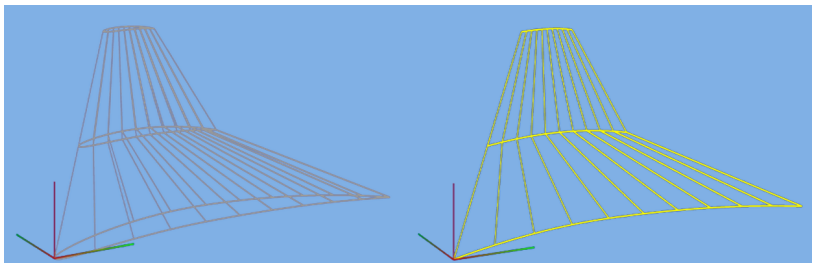

Figure 2.5: Example of mean surface creation

As mentioned before, there are several methods for the construction of the mesh for this problem. Though the derivatives require the evaluation of $z$ for the mean surface

at the $x$ and $y$ coordinates of a certain control point, the actual $z$ coordinate of that particular control point depends on the location of the elemental panel it belongs to. The code developed allows three distinct ways of placing them (Figure 2.6). The first

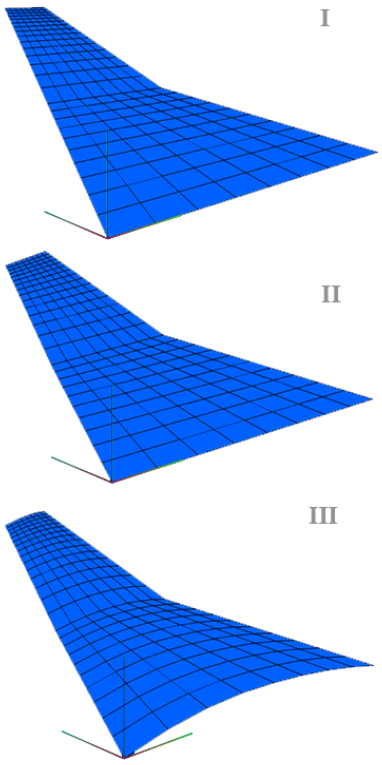


Figure 2.6: Elemental panel layup options

option forces all the panels to lie on a flat surface, which means all of the $z$ coordinates of the control points will be zero. In the second option the surface follows the dihedral and twist of the wing. In the third one, it goes beyond that and effectively coincides with the mean surface of the wing, which, in general, is cambered. The latter, though obviously more accurate, specially for highly cambered airfoils, comes of course at an additional computational cost.

## 2.2 Compressibility correction

Due to the assumption of incompressible flow, in order to simplify the solution, it is required that we apply a compressibility correction according to the freestream Mach number ($M_\infty$) [18], otherwise the accuracy of the solution will suffer. Usually, compressibility effects come into play beyond $M_\infty = 0.3$. The simplest correction to apply is the Prandtl-Glauert rule, which consists of applying a transformation to the geometry along the $x$-axis. More specifically, the equivalent wing in incompressible flow is a lengthened version of the original one, stretched by a factor $\beta = \sqrt{1 - M_\infty^2}$ [18]. This rule allows the expansion of the envelope within which it is reasonable to analyze a straight untapered wing with VLM codes up to $M_\infty \approx 0.7$. After this point, the appearance of supersonic flow regions across the wing is almost certain (i.e., the critical Mach number is reached). For swept wings, however, this envelope may be further extended, since it is the effective Mach number ($M_{eff}$) that characterizes the flow, rather than $M_\infty$ (Figure 2.7) [23].

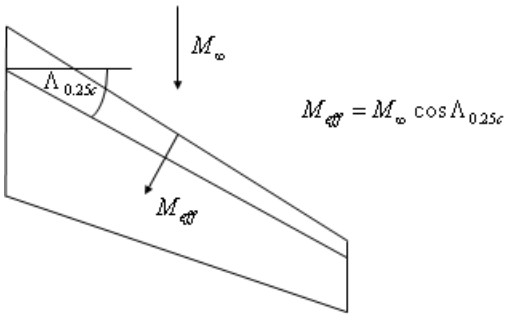


Figure 2.7: Sweep and effective Mach number

## 2.3 Friction and form drag

As noted earlier, the vortex lattice method does not account for skin friction, nor form drag. Therefore, an empirical approach implemented by Mason [24] is employed, albeit with some modifications. The procedure for skin friction drag estimation is detailed in Appendix B, but the basic relation is:

$$C_{D_f} = C_f FF \frac{S_{wet}}{S_{ref}} \tag{2.8}$$

where $C_f$ is the coefficient of friction, accounting for a laminar/turbulent boundary layer flow developing across the wing [1], and $FF$ is the form factor, which is essentially an empirical correction to take into consideration the airfoil shape and possible flow separation [25] (again, both computed as in Appendix B). The computation of the friction coefficient also takes compressibility into account. One of the main assumptions is that this base drag does not vary significantly for small angles of attack.

## 2.4 Prediction of maximum lift coefficient

The maximum coefficient of lift of a wing is crucial to have an idea of the take-off and landing performance of an aircraft. It may be estimated by evaluating the local $C_l$ of several wing sections at two different angles of attack in order to extrapolate their (assumed linear) behavior until stall (to that end, the user supplied maximum sectional lift coefficients for the three different airfoils that compose the wing are interpolated). The section that stalls at the lowest angle of attack dictates the stall angle of attack of the wing and thus its $C_{L_{max}}$. It is then just a matter of correlating

[1] The value of the expected transition Reynolds number - $Re_{trans}$ - should be provided. Typical values range between $5 \times 10^5$ and $1 \times 10^6$.

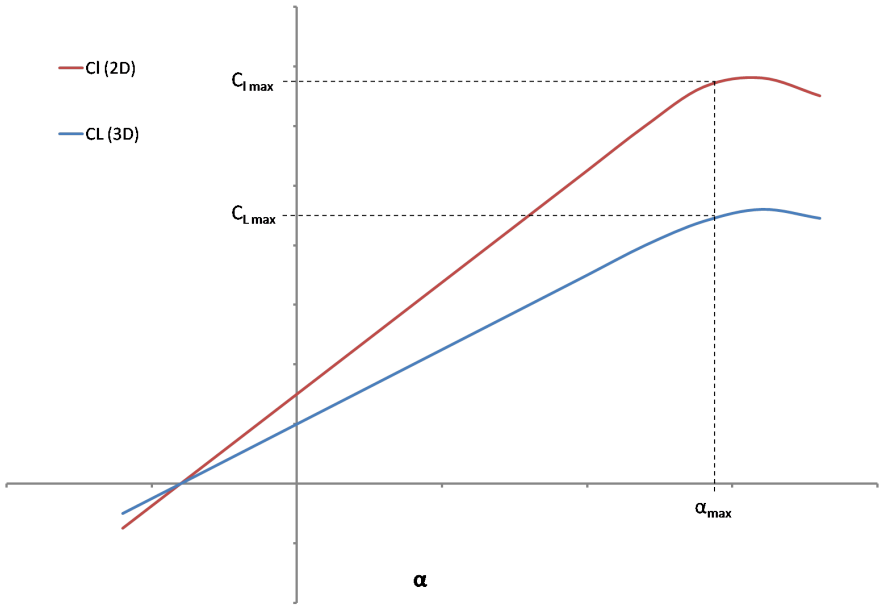


Figure 2.8: Determination of wing $C_{L_{max}}$

the sectional lift distribution with the overall $C_L$ of the wing.

Other effects of the complex three dimensional flow over a wing at high angles of attack might of course come into play but this is usually a decent alternative to complex CFD in order to get a first order approximation [26].

## 2.5 Validation

In order to validate this analyzer module, which was named *Zephyr*, comparison with other already validated codes and/or experimental data is required. To that end, a series of cases will be presented, spanning very different configurations and flight conditions.

### 2.5.1 Test Case 1: Warren 12 planform

The Warren 12 planform (shown in Figure 2.9) is presented in [19] as a benchmark for VLM codes, which is why it is an obvious first choice. The dimensions are as follows (in meters):

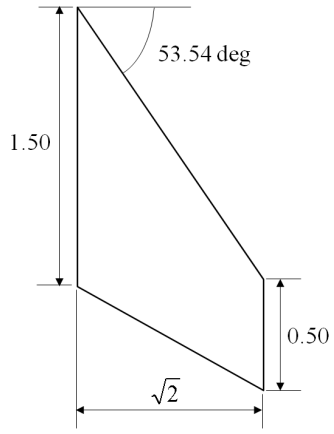


Figure 2.9: Warren 12 planform

The results are obtained with a 17×24 panels mesh (chordwise×spanwise), totaling 408 panels (computation time is under 4 seconds in a Pentium 4 desktop computer at 3.4Ghz):

Table 2.1: Comparison of results for the Warren 12 planform

| | **Warren 12** | ***Zephyr*** | **Error[%]** |
|---|---|---|---|
| $C_{L_\alpha}$ [rad$^{-1}$] | 2.743 | 2.755 | 0.4 |
| $C_{M_\alpha}$ [rad$^{-1}$] | -3.100 | -3.116 | 0.5 |

These results[1] reveal a very good agreement between the benchmark standard and the code developed, both in terms of the evaluation of the lifting effects and their distribution across the wing. The latter can be inferred from the fact that the error in the coefficient of moment is also very low, which means the loads are bound to be correctly distributed across the wing.

Because this wing has a flat surface, inputting any symmetrical airfoil will yield the same values (remember that the vortex lattice method ignores thickness, Sec. 2.1.1). The values presented above are calculated for a run at a 5 deg angle of attack (the code actually executes another run at $\alpha = 4$ deg to compute the derivatives, assuming a locally linear behavior of the wing).

### 2.5.2 Test Case 2: Comparison with TORNADO

Developed as a MATLAB program, TORNADO (version 1.30b) is a vortex lattice code which displays advanced features such as the bending of the vortex wake aft of the wing and the computation of both longitudinal and lateral stability derivatives, including those with respect to angular rates [27]. It is also versatile in the way that it allows configurations of multiple complex surfaces. Major downsides though, are the unavailability of any kind of compressibility corrections, thus preventing its use but at the low subsonic regime, as well as being computationally very slow when

[1]The results for $C_{M_\alpha}$ were obtained using the mean geometric chord rather than the MAC, that *Zephyr* uses by default. Also, in *Zephyr*, $C_M$ is always computed with respect to the apex of the wing.

compared to *Zephyr*.

Because of TORNADO's versatility, a more intricate wing configuration was chosen to perform the comparison. Figure 2.10 depicts the planform used in the calculations. The airfoils used were NACA 5405, 5506 and 4607 for the root, break station and tip, respectively (Tornado only allows NACA airfoils to be loaded automatically). The twist at the tip is 10 deg whereas at the break station no twist is applied. Dihedral angle is positive by 4 deg.

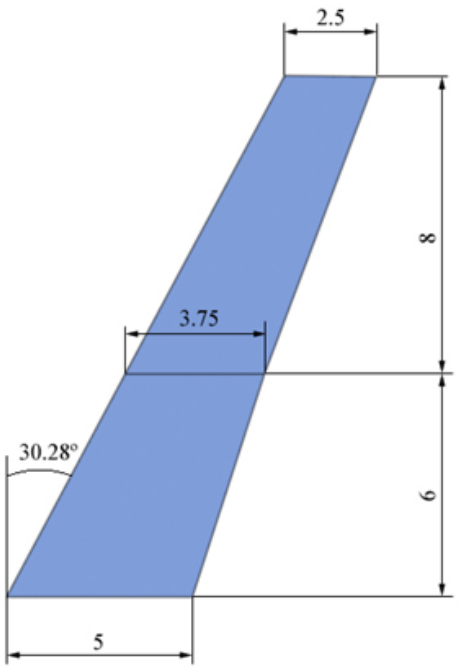


Figure 2.10: Planform for Test Case 2

Flight conditions were set as $\alpha = 5$ deg, $V_\infty = 60$ m/s (of course, $M_\infty = 0$, for comparison purposes), at sea level conditions. Because TORNADO uses a mesh without camber, the results here presented are for a Type II (see Sec. 2.1.2) mesh in *Zephyr* (18x24).

Table 2.2: Comparison with TORNADO

| | **TORNADO** | ***Zephyr*** | **Error[%]** |
|---|---|---|---|
| $C_L$ | 0.6907 | 0.6898 | 0.1 |
| $C_{D_i}$ | 0.0201 | 0.0197 | 2.0 |
| $C_M$ | -0.9150 | -0.9196 | 0.5 |

Again, a good correlation is obtained between the codes. Some of the differences may be explained through the fact that TORNADO computes the normals in Eq. 2.2 using the geometry of the panels directly (by means of a cross product [27]), i.e., without ever resorting to computing the gradient. This method, though expedient, is certainly less accurate, since the curvature of the surface is not being accurately captured. The spline interpolation and differentiation as in the current approach has a higher fidelity. Further comparison is possible since both codes are capable of outputting both the pressure distribution across the surface as well as the sectional coefficient of lift along the span (Figure 2.11).

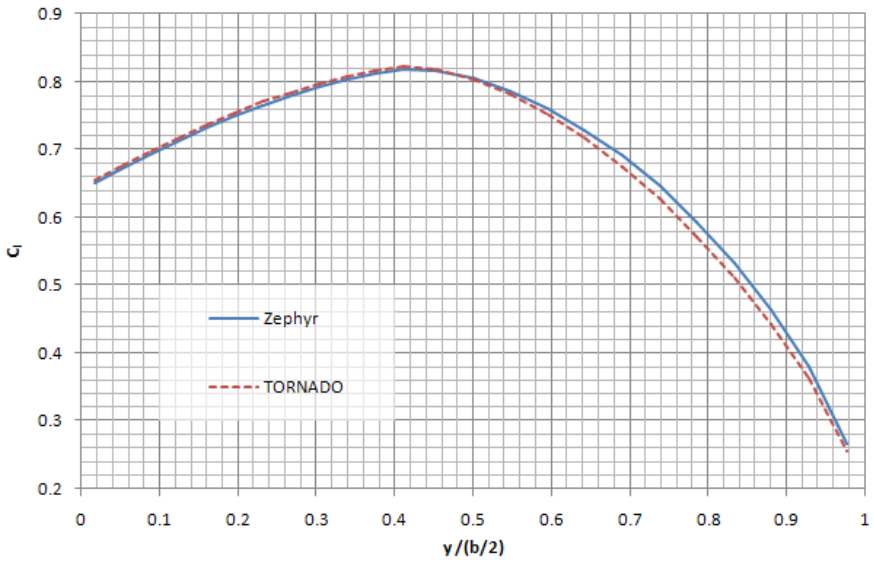


Figure 2.11: Section $C_l$ vs. semispanwise nondimensional coordinate

Though the results are very similar, the small discrepancy on the outboard portion of the wing (noticeable in Figure 2.11) may reveal yet another difference in implementation between *Zephyr* and TORNADO, in the way the twist is applied to the wing. In *Zephyr*, twist is applied so that a section rotates about the trailing edge of the wing [28] (so that, for instance, a rectangular wing with twist would keep a straight trailing edge). The approach followed by TORNADO is unknown.

### 2.5.3 Test Case 3: Comparison with OVERFLOW

This last test case was run with the aim to validate both the compressibility correction and viscous/form drag computation. Experimental data with both a clear definition of the geometry and sufficiently detailed results to allow a comparison to be made was found to be scarce. This lead to a computational work developed by Chao and Dam [29] being used as a benchmark. The aforementioned paper describes the analysis of the flow over a wing using OVERFLOW, a RANS (Reynolds Averaged Navier-Stokes) CFD solver. The geometry of the test wing is presented in Figure 2.12, the NACA 0012 being the airfoil used for all sections.

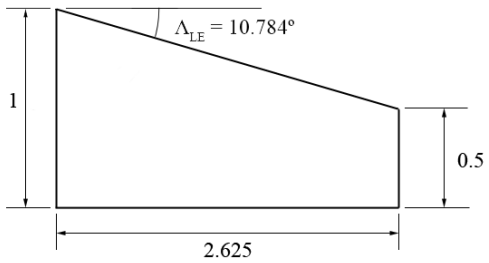


Figure 2.12: Planform for Test Case 3

Two distinct flight conditions were run: one at $M_\infty = 0.25$ and another one at

$M_\infty = 0.73$, both sharing the same angle of attack ($\alpha = 4$ deg) and Reynolds number ($10^6$, with the root chord as the reference length, according to [29]). In order to maintain $Re$ at this value, flight altitude had to be set at 14950 m and 21730 m for the first and second runs, respectively. Full turbulent flow is specified and therefore $Re_{trans}$ is arbitrarily set at a low value such as 1 (a value of zero would make some of the expressions in Appendix B singular).

Table 2.3: Comparison with OVERFLOW

| | $M_\infty = 0.25$ | | | $M_\infty = 0.73$ | | |
|---|---|---|---|---|---|---|
| | **Chao/Dam** | ***Zephyr*** | **Error[%]** | **Chao/Dam** | ***Zephyr*** | **Error[%]** |
| $C_L$ | 0.3240 | 0.3266 | 0.8 | 0.4160 | 0.4097 | 1.5 |
| $C_{D_i}$ | 0.0046 | 0.0047 | 2.2 | 0.0075 | 0.0071 | 5.3 |
| $C_{D_f}$ | 0.0107 | 0.0119 | 11.2 | 0.0116 | 0.0116 | 0.0 |
| $C_{D_{wave}}$ | - | - | - | 0.0055 | - | - |

A good agreement is obtained in terms of lift and induced drag, even for the higher Mach number, which is at the limit of the validity for the Prandtl-Glauert correction. Nevertheless, for friction and form drag, somewhat expectedly given the empirical nature of the method employed, the results at $M_\infty = 0.25$ differ by over 10%. The coincidence observed for $M_\infty = 0.73$ for $C_{D_f}$ is surprising. Zephyr does not account for wave drag, ($C_{D_{wave}}$), so a comparison in this area cannot be made. In spite of all this, the accuracy of the aerodynamic solver may be deemed acceptable at the preliminary design stage.

# Chapter 3

# Structural/Aeroelasticity Solver

In this chapter, we discuss the implementation of a structural analyzer module based on the Equivalent Plate Model (EPM) Theory for aircraft wings. Several implementations in this area have lead to expedited ways of evaluating the aerolelastic behavior of complex wing structures, without resorting to more cumbersome finite element models [30], [31], [32], [33], [34], including a nonlinear approach by Livne et al. [35]. These are generally based either on the Classical Plate Theory (CPT) or the First-order Shear Deformation Theory (FSDT). A review of these theories, among others, is presented in [36]. One of the major downsides of the EPM approach, especially when compared with FEM, is that all information concerning the distribution of stresses is lost when simplifying the geometry to create the equivalent plate. Therefore it is very difficult to come up with an estimate for the safety factor (e.g., based on the material's yield stress) for a certain configuration.

In this section, along with a brief description of the theory, the focus will be set upon describing the various design variables associated with the structure as well as how this module will interact with the rest of the tool.

## 3.1 Equivalent Plate Theory and Implementation

The implementation of this theory by R. Gabriel [37] is mainly based on the work of Kapania and Liu [30], in which FSDT was applied to create an EPM of a wing. A computer code (*Awing*) was then developed in FORTRAN to evaluate the performance of the structure according to such a model.

The current work was then about creating the means for this code to interact with the remaining modules of the MDO framework.

### 3.1.1 Mathematical formulation

While full details on the formulation of these equivalent models are available in [37] and [30], an outline of the methodology will be presented next. There are two main assumptions to this formulation: a line normal to the non-deformed mid-surface remains straight after deformation, and the transverse normal stress may be neglected in the constitutive equations. Therefore, the displacement field has the following form (recalling the coordinate system presented in Figure 1.1):

$$\begin{aligned} u(x,y,z,t) &= u_0(x,y,t) + z\phi_x(x,y,t) \\ v(x,y,z,t) &= v_0(x,y,t) + z\phi_y(x,y,t) \\ w(x,y,z,t) &= w_0(x,y,t) \end{aligned} \tag{3.1}$$

$u$, $v$ and $w$ are displacements, and $\phi_x$ and $\phi_y$ are rotations about the $x$ and $y$ axis, respectively. The strains are given by:

$$\begin{aligned}
\epsilon_1 &= \epsilon_{xx} = \frac{\partial u}{\partial x} = \frac{\partial u_0}{\partial x} + z\frac{\partial \phi_x}{\partial x} \\
\epsilon_2 &= \epsilon_{yy} = \frac{\partial v}{\partial y} = \frac{\partial v_0}{\partial y} + z\frac{\partial \phi_y}{\partial y} \\
\epsilon_3 &= \epsilon_{zz} = \frac{\partial w}{\partial z} = 0 \\
\epsilon_4 &= \gamma_{xy} = 2\epsilon_{xy} = \frac{\partial u}{\partial y} + \frac{\partial v}{\partial x} = \frac{\partial u_0}{\partial y} + \frac{\partial v_0}{\partial x} + z\left(\frac{\partial \phi_x}{\partial y} + \frac{\partial \phi_y}{\partial x}\right) \\
\epsilon_5 &= \gamma_{yz} = 2\epsilon_{yz} = \frac{\partial v}{\partial z} + \frac{\partial w}{\partial y} = \phi_y + \frac{\partial w_0}{\partial y} \\
\epsilon_6 &= \gamma_{zx} = 2\epsilon_{zx} = \frac{\partial w}{\partial x} + \frac{\partial u}{\partial z} = \phi_x + \frac{\partial w_0}{\partial x}
\end{aligned} \tag{3.2}$$

The internal energy of the system is:

$$U = \frac{1}{2}\iiint_V \sigma_{ij}\epsilon_j dV = \frac{1}{2}\iiint_V \epsilon_i D_{ij}\epsilon_j dV \tag{3.3}$$

where the constitutive relations for the material (Hooke's Law, establishing the relation between the stress state $\sigma_{ij}$ and the strains $\epsilon_i$) were applied in the form of the tensor $D_{ij}$ (taken as symmetrical).

On the other hand, for the kinetic energy of the equivalent plate we have:

$$T = \frac{1}{2}\iiint_V \rho\, \mathbf{v}.\mathbf{v} dV \tag{3.4}$$

$\mathbf{v}$ being the velocity vector:

$$\mathbf{v} = \left(\frac{\partial u_0}{\partial t} + z\frac{\partial \phi_x}{\partial t}, \frac{\partial v_0}{\partial t} + z\frac{\partial \phi_y}{\partial t}, \frac{\partial w_0}{\partial t}\right) \tag{3.5}$$

In order to perform the calculations, however, the general wing geometry needs to be transformed into the square domain defined by $\xi$, $\eta$:

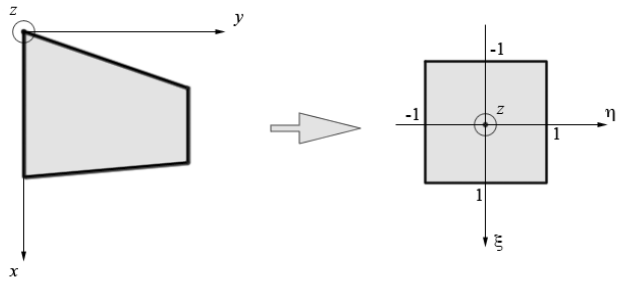


Figure 3.1: Domain transformation

The application of such transformation and subsequent discretization of Eqs. (3.3) and (3.4) leads to a rather lengthy derivation which goes beyond the scope of the current work (but is again duly explained in [37] and [30]). In order to evaluate the integrals in the aforementioned equations, Gaussian quadrature is used. The integrands and limits of integration are defined by the geometry of the wing and the properties of its structural elements (which are the topic of Sec. 3.2).

### Static deformation

To compute the static deformation of the structure, the work done by external forces must be calculated:

$$Q = \iint \mathbf{P}\,(x, y, t)\,.\,(u, v, w)\,dxdy \tag{3.6}$$

The displacement and rotation functions are then approximated by Ritz weighting functions and the integrals in Eqs. (3.3) and (3.4) are evaluated so that the following

system of equations is obtained:

$$K_{ij}q_j = P_i \tag{3.7}$$

Where $K_{ij}$ is the stiffness matrix obtained through integration of Eq. (3.3), $q_j$ is the generalized displacement vector (weighting the Ritz functions) and $P_i$ is the generalized load vector.

In *Awing*, the loading input is actually the output from the aerodynamics module (*Zephyr*), which generates a distribution of point loads across the wing surface.

**Natural vibration**

Solving the generalized eigen-value problem:

$$\left(K_{ij} - \omega^2 M_{ij}\right) x_j = 0 \tag{3.8}$$

allows the computation of natural vibration frequencies and modes, $M_{ij}$ is the mass matrix resulting from the evaluation of the integral in Eq. (3.4), $\omega^2$ is the eigen value (natural frequency squared), and finally, $x_j$ is the eigen vector representing the mode shape.

## 3.2 Definition of structural design variables

The assembly of the stiffness and mass matrices for the equivalent plate requires information from four major groups of structural components: spars, rib, stringers and skins. The set of material properties taken into consideration allows the definition a wide array of material types, both isotropic and orthotropic, including most types of composite layups.

The current version of *Awing* has two major limitations: only one airfoil section is allowed and only trapezoidal, untwisted wings without dihedral are supported. The main consequence is that not all of the geometric parameters can be taken as design variables in an aero-structural optimization.

The following sections aim to describe what information on the geometric and material properties of these elements is carried through to the structural/aeroelasticity module and to the optimizer. Note that in the current approach, the material type itself, and hence its properties, are not taken into consideration as design variables (though this might change in a future revision).

### 3.2.1 Spars

Spars usually present the greatest contribution to a wing's bending stiffness. In the present case, they extend from root to tip, their placement at those locations being defined as a fraction of the respective chord (Figure 3.2). For the current

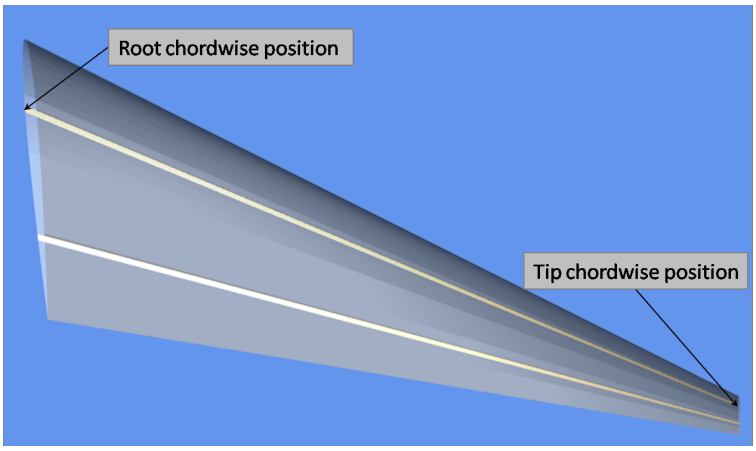


Figure 3.2: Spars positioning

implementation, spars are taken as I-beams, their sections being defined as seen in Figure 3.3. These dimensions are allowed to vary linearly from root to tip.

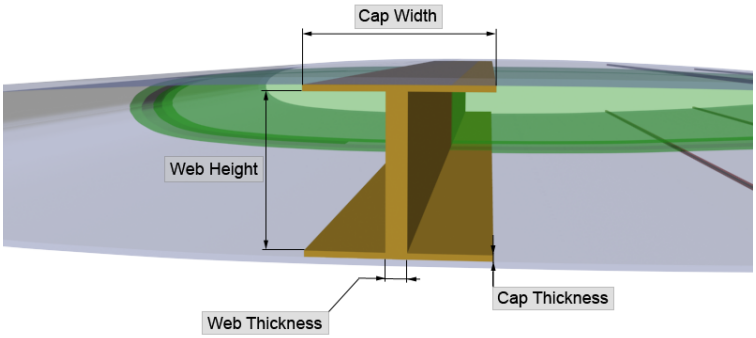


Figure 3.3: Spar section dimensions

Different materials may be specified for the cap and web of the spar. The material properties taken into consideration are defined by the parameters portrayed on Table 3.1.

Table 3.1: Material properties definition for spars

| **Material property** | **Units** | **Obs.** |
|---|---|---|
| Web | | |
| Longitudinal elastic modulus, $E_{web}$ | Pa | |
| Shear Modulus, $G_{web}$ | Pa | |
| Poisson ratio, $\nu_{ez}$ | | $e$ means the longitudinal direction |
| Poisson ratio, $\nu_{ze}$ | | $e$ means the longitudinal direction |
| Density, $\rho_{web}$ | kg.m$^{-3}$ | |
| Cap | | |
| Longitudinal elastic modulus, $E_{cap}$ | Pa | |
| Poisson ratio, $\nu_{ez}$ | | $e$ means the longitudinal direction |
| Poisson ratio, $\nu_{ze}$ | | $e$ means the longitudinal direction |
| Density, $\rho_{cap}$ | kg.m$^{-3}$ | |

### 3.2.2 Ribs

Ribs, being placed transversally in the wing, are responsible for a substantial contribution to a wing's torsional stiffness but they exist primarily to support the skin and prevent it from buckling. The rib section properties are sketched in Figure 3.4 and they are specified both at the leading and trailing edges.

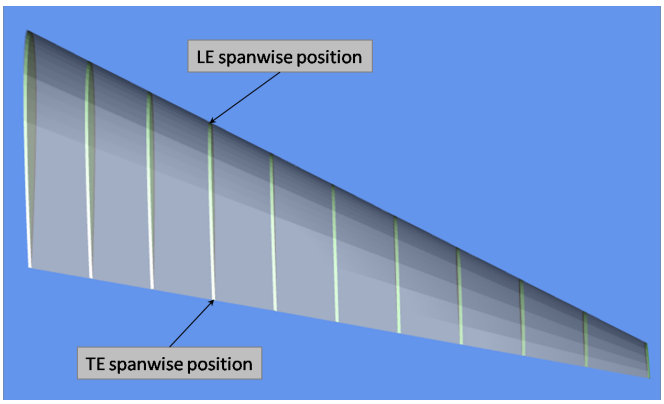


Figure 3.4: Ribs positioning

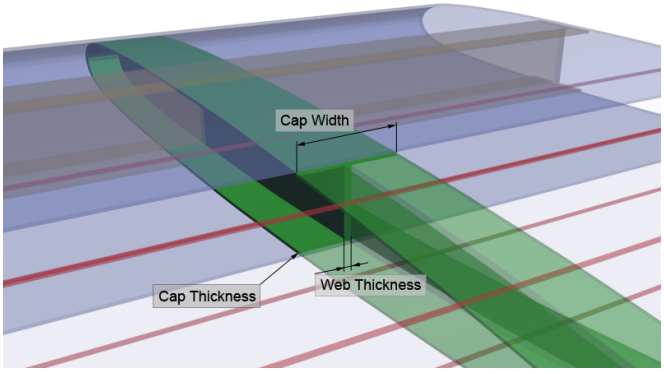


Figure 3.5: Rib section dimensions

Much like what happens for spars, different materials can be specified for cap and

web.

Table 3.2: Material properties definition for ribs

| **Material property** | **Units** | **Obs.** |
|---|---|---|
| Web | | |
| Longitudinal elastic modulus, $E_{web}$ | Pa | |
| Shear Modulus, $G_{web}$ | Pa | |
| Poisson ratio, $\nu_{ez}$ | | $e$ means the longitudinal direction |
| Poisson ratio, $\nu_{ze}$ | | $e$ means the longitudinal direction |
| Density, $\rho_{web}$ | kg.m$^{-3}$ | |
| Cap | | |
| Longitudinal elastic modulus, $E_{cap}$ | Pa | |
| Poisson ratio, $\nu_{ez}$ | | $e$ means the longitudinal direction |
| Poisson ratio, $\nu_{ze}$ | | $e$ means the longitudinal direction |
| Density, $\rho_{cap}$ | kg.m$^{-3}$ | |

### 3.2.3 Stringers

Stringers are reinforcements placed on the skin that further add to the bending stiffness of the wing and also help in preventing the buckling of the skin. Their effectiveness is due to their relatively high sectional moment of inertia since their placement is by nature far away from the wing section centroid.

Placement of stringers on the wing is defined in Figure 3.6 and they are defined in pairs (sharing the same chord fraction, one at the upper surface and another at the lower one). Each stringer's section is defined by its height and width as seen in Figure 3.7. A single material type is defined for stringers.

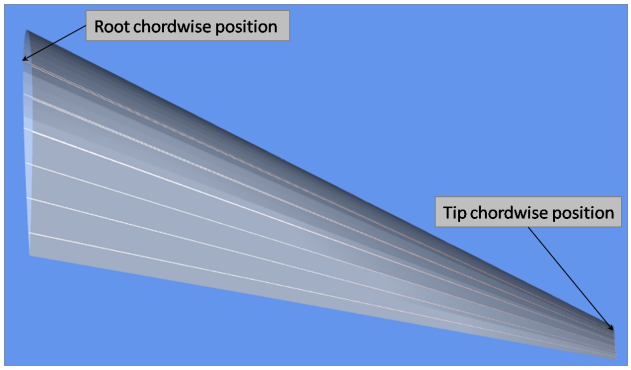


Figure 3.6: Stringers positioning

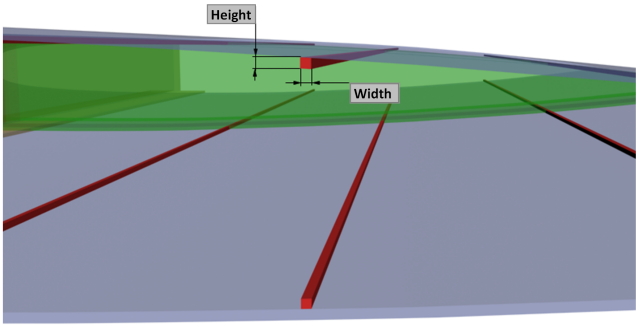


Figure 3.7: Stringer section dimensions

Table 3.3: Material properties definition for stringers

| **Material property** | **Units** | **Obs.** |
|---|---|---|
| Longitudinal elastic modulus, $E$ | Pa | |
| Shear Modulus, $G$ | Pa | |
| Poisson ratio, $\nu_{ez}$ | | $e$ means the longitudinal direction |
| Poisson ratio, $\nu_{ze}$ | | $e$ means the longitudinal direction |
| Density, $\rho$ | kg.m$^{-3}$ | |

### 3.2.4 Skin panels

The skin not only gives the wing its aerodynamic shape but may also contribute significantly to both its bending and torsional stiffness. As a matter of fact, some

wing designs rely solely on the skin as their structural element.

The skin panels placement on the wing is defined by the front and aft chord fractions at root and tip (Figure 3.8). Much like stringers, they are defined in pairs, which share the same properties except that one is placed at the upper surface and another one at the lower surface of the wing. As to the assignment of thicknesses and material properties, these are explained through Figure 3.9 and Table 3.4.

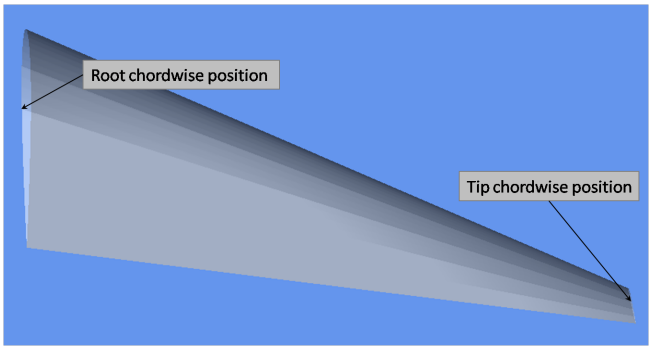


Figure 3.8: Placement of skin panels

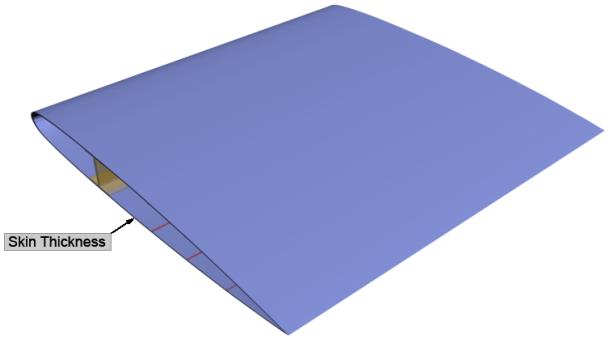


Figure 3.9: Definition of skin thickness

Table 3.4: Material properties definition for skin panels

| **Material property** | **Units** | **Obs.** |
|---|---|---|
| In-plane elastic modulus, $E_X$ | Pa | in global coord. system |
| In-plane elastic modulus, $E_Y$ | Pa | " |
| In-plane shear modulus, $G_{XY}$ | Pa | " |
| Normal shear modulus, $G_{XZ}$ | Pa | " |
| Normal shear modulus, $G_{YZ}$ | Pa | " |
| Poisson ratio, $\nu_{xy}$ | | " |
| Poisson ratio, $\nu_{yx}$ | | " |
| Density, $\rho$ | kg.m$^{-3}$ | |

## 3.3 Validation

A validation of the structural code was performed in [37], by comparing it with similar codes as well as with finite element models. The results from the latter are presented here since they are the most meaningful to the current work.

Tables 3.5 and 3.6 contain the details of the wing used for this analysis. The internal structure is composed of 4 spars and 11 ribs made of aluminum. The skin is also made of aluminum and is defined by two skin panels covering its upper and lower parts.

The airfoil presented is obtained through a Karman-Treftz conformal transformation [37].

For the analysis under static loads, a pair of loads, equal in magnitude (10000 N) and opposite in direction was applied at the wing tip (at the locations of the first and last spars). The results when compared to the corresponding finite element model in ANSYS® are presented in Figure 3.10. Though the computed solution seems to capture the general tendency of the displacement field, it is also apparent that this approach suffers from a lack of fidelity for increasingly complex structures (simpler

Table 3.5: Description of wing for structural test case (planform)

| **Planform dimension** | **Value** |
|---|---|
| Semispan, $\frac{b}{2}$ | 4.88 m |
| Break station, $bs$ | 2.44 m |
| LE Sweep, $\Lambda_{LE}$ | 30 deg |
| Tip twist | 0 deg |
| Break station twist | 0 deg |
| Dihedral, $\varphi$ | 0 deg |
| Root chord, $c_r$ | 1.83 m |
| Break station chord, $c_{bs}$ | 1.37 m |
| Tip chord, $c_t$ | 0.91 m |
| Airfoil | |

Table 3.6: Description of wing for structural test case (structure)

| **Structural variable** | **Value** | **Obs.** |
|---|---|---|
| Spar chord fraction | 0.2/0.4/0.6/0.8 | root and tip |
| Spar web thickness | 1.47 mm | root and tip |
| Spar cap height | 5.00 mm | root and tip |
| Spar cap width | 9.47 mm | root and tip |
| Rib semispan fraction | 0.0909/0.1818/0.2727/0.3636/ 0.4545/0.5455/0.6364/0.7273/ 0.8182/0.9091/1.0 | LE and TE |
| Rib web thickness | 1.47 mm | LE and TE |
| Rib cap height | 5.00 mm | LE and TE |
| Rib cap width | 9.47 mm | LE and TE |
| Skin thickness | 3.0 mm | |
| Skin thickness ratio | 1.0 | |

cases discussed in [37] yielded better results). On the other hand, the modal analysis presented a much better agreement with the finite element model, as evidenced by Table 3.7.

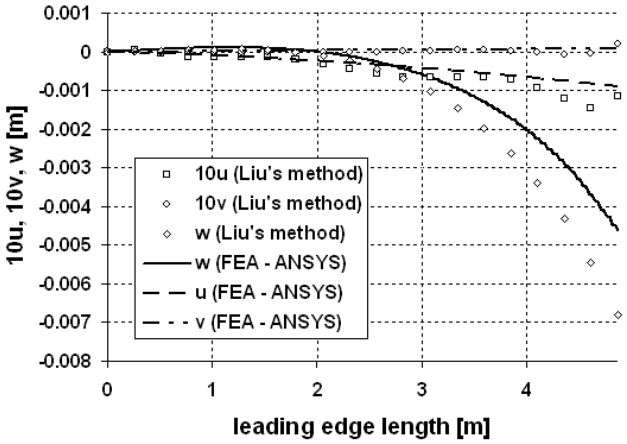


Figure 3.10: Displacement field evaluated at the leading edge [37]

Table 3.7: Comparison of natural vibration frequencies

| Mode | *Awing* [rad.s$^{-1}$] | FEM [rad.s$^{-1}$] | Error [%] |
|---|---|---|---|
| 1$^{st}$ | 46.451 | 46.639 | 0.40 |
| 2$^{nd}$ | 203.408 | 200.068 | 1.67 |
| 3$^{rd}$ | 280.541 | 284.249 | 1.30 |
| 4$^{th}$ | 371.215 | 358.933 | 3.42 |
| 5$^{th}$ | 496.568 | 458.022 | 8.42 |
| 6$^{th}$ | 744.267 | 726.960 | 2.38 |

All in all, the price paid in terms of accuracy of the solution, especially in terms of static deformation, is more than outweighed by the simplicity in parameterizing the structure and the computational cost of such an implementation when compared with a equivalently detailed finite element model. There is no doubt, however, that these accuracy issues should be the object of future work on this module.

## 3.4 Aeroelasticity

Aeroelasticity is the study of the interaction of an elastic structure with it's fluid surroundings. This interaction may lead to disastrous results if it is not adequately predicted and no steps are taken to control it.

### Static Aeroelasticity

The static deformation of a wing in flight under the aerodynamic loads may be considered as an aeroelastic phenomenon. For a constant $C_L$, there will be a divergence speed, $V_d$, at which the twisting caused by the moment of the lift forces (essentially) about the centre of twist of the wing will overcome the torsional stiffness of the structure, causing it to fail. In aft-swept wings, the bending of the wing is usually beneficial in terms of divergence, by alleviating the torsion at a certain section (the wing incidence is actually reduced as the wing twists). Conversely, in forward swept wings the effect is the opposite [38], hence the lower divergence speeds observed for this type of wings.

### Dynamic Aeroelasticity

On the other hand, a phenomenon known as flutter consists of the dynamic interaction between the structure itself and the aerodynamic loads imposed by the surrounding air stream. Although types of flutter based on excitation of pure bending or pure torsion modes are stable and hence harmless, the same does not hold true for cases where these types of motion coexist, but with a certain phase difference - classical flutter. A common example is presented in Figure 3.11, bestowing a 90 degree phase difference between bending and torsion modes.

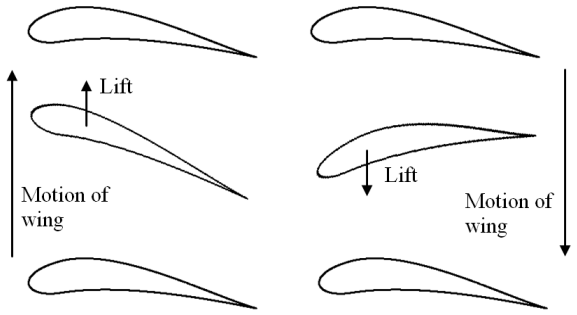


Figure 3.11: Classical flutter

It is immediately apparent that while crossing the equilibrium position in bending, the wing suffers both maximum and minimum lift loads due to the twist-increased/ decreased angle of attack. The fact that these loads are synchronous with the motion of the wing means that at a given speed, $V_f$ (flutter speed), the aerodynamic loads surpass the admissible values and the oscillations quickly diverge, eventually leading to structural collapse. Other types of flutter, often referred to as non-classical flutter, include aileron buzz, buffeting and stalling flutter.

### 3.4.1 Implementation

Based on the knowledge of natural frequencies of the wing structure, such as those obtained through *Awing*, it is possible to derive semi-empirical expressions to predict flutter speed. The MDO tool developed makes use of the relations introduced in [39] and [40], in order to estimate the flutter speed.

$$V_f = \frac{\omega_\alpha \, r_\alpha}{\sqrt{4\pi\rho\,\epsilon\frac{\frac{b}{2}}{m_{wing}}}} \tag{3.9}$$

$$V_f = \frac{\omega_\alpha \, r_\alpha}{\sqrt{2 \, C_{L_\alpha} \, \rho \, \epsilon \frac{\frac{b}{2}}{m_{wing}}}} \tag{3.10}$$

In the above, $\omega_\alpha$ is the first uncoupled torsional frequency of the wing structure, $r_\alpha$ is the radius of gyration of the wing expressed as a fraction of the average semi-chord, $\rho$ is the freestream air density, and $\epsilon$ is the distance from the wing section center of mass to the aerodynamic center (1/4 chord) as a fraction of the chord. The values of $r_\alpha$ and $\epsilon$ are difficult to obtain for more general wing structures such as the ones being treated here. To that end, the user has control over these parameters, which are by default estimated to be $r_\alpha = 0.5$ and $\epsilon = 0.25$ [40].

Eqs. 3.9 and 3.10 are essentially equivalent, save for the fact that the latter accounts for the actual lift curve slope of the wing, rather than using the crude approximation of Eq. 3.9, in which the value of $2\pi$ is used ($2\pi$ being the lift curve slope of an infinite flat plate in potential flow). This approximation, however, has the advantage of requiring a single aerodynamics evaluation in comparison the two needed for the computation of $C_{L_\alpha}$.

The validity of these expressions is constrained to trapezoidal wings, furthermore since the uncoupled torsional frequency and wing mass are calculated using *Awing* which in itself is limited to that type of planform.

# Chapter 4

# Graphical User Interface

In this work, there is also an interest in how the user should interact and easily formulate wing optimization problems. Therefore, an interface was created to assist in the operation of this application. The GUI was developed using the C# object-oriented language as it facilitates the process of setting up the various elements of a graphical interface (windows, menus, buttons...) as compared to Visual C++, for example. One of the requirements of such an interface was, however, to make it modular, so that the various analyser/optimizer modules could be easily interchanged. To that end, provisions were made so that these modules can be accompanied by a suitable interface which serves as a bridge between the user interface itself and the underlying analyser module. Furthermore, if the module in question is compiled as an application extension (dynamic-link library, .dll), input and output procedures are performed much faster since all data is exchanged through system memory (RAM) rather than through files (and therefore using the much slower hard drives). To exemplify this procedure, the aerodynamics module (*Zephyr*, which was coded in C++) was converted to such an extension and the respective interface was created to allow communication with the main application. The optimizer developed in MATLAB

is also compiled as a dynamic-link library, though it requires the installation of the MATLAB® Component Runtime (MCR) in order to function properly.

The interface is divided into 7 main tabs, each of them dedicated to a specific task. These are: Geometry, Aerodynamics, Structure, Aeroelasticity, Cost (not yet implemented, which will allow for the development of a future cost estimation module), Optimization and Other results. Most of these sections are equipped with a 3D viewer for which a DirectX® graphics engine was developed. This viewer presents the ubiquitous zoom, pan and rotate capabilities.

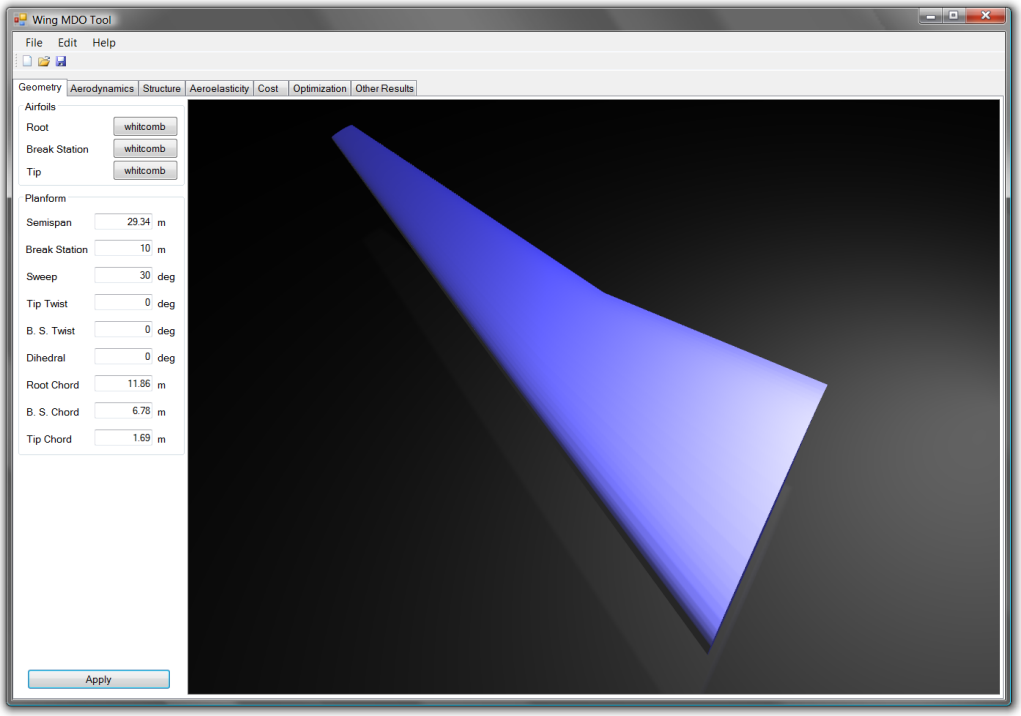


Figure 4.1: Geometry screen

Figure 4.1 displays the Geometry tab, where the values for the parameters that define the shape of the baseline wing may be entered (Sec 2.1.2). There are also

buttons that call dialog boxes allowing three distinct airfoils to be loaded. In this case the 3D viewer window will display the current baseline configuration.

The Aerodynamics tab (Figure 4.2) is prepared for the analysis of the wing at user specified flight conditions. Other controls include the specification of the maximum $C_l$ for each of the three airfoil sections previously defined and the mesh settings.

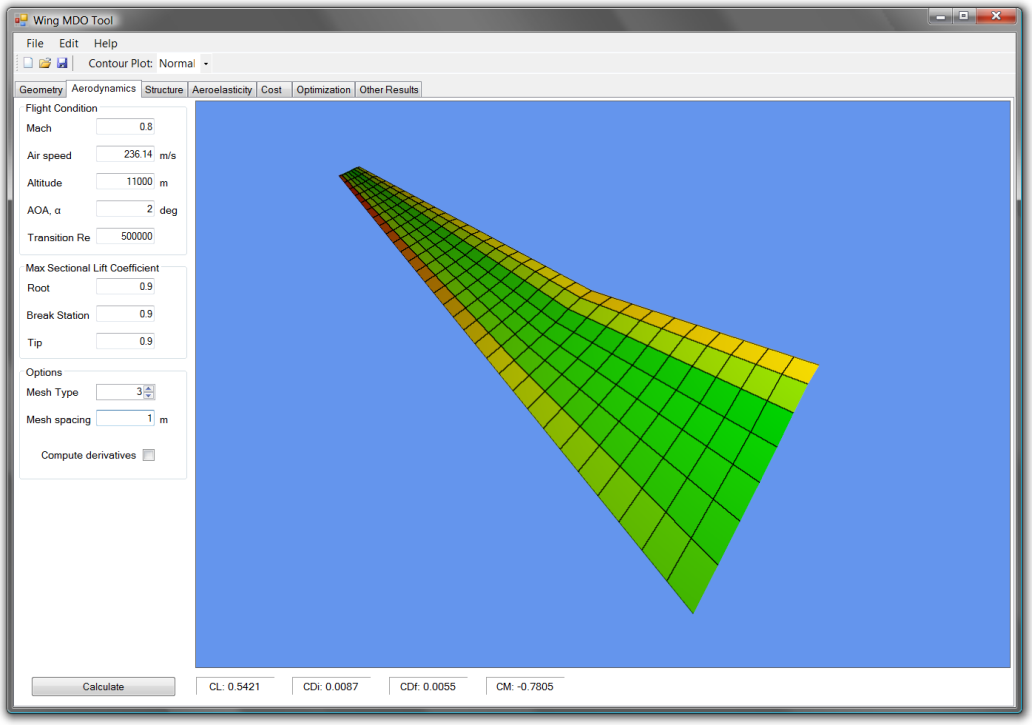


Figure 4.2: Aerodynamics screen

Upon execution of the VLM, the 3D viewer displays the pressure distribution over the wing. At the bottom, the main non dimensional coefficients of interest are shown.

The structure tab (Figure 4.3) allows the definition of the internal structure of the wing for later analysis. It requires the geometry to be defined in advance. Structural elements and their respective properties are defined by means of pop-up menus such as

the one on Figure 4.4. A tree-view control on the left hand side was also implemented to define and keep track of all the structural elements. In this screen the 3D viewer will display a three-dimensional mock up of the wing structure including spars, ribs, stringers and skins. In order to reduce clutter, four buttons on the top of the window

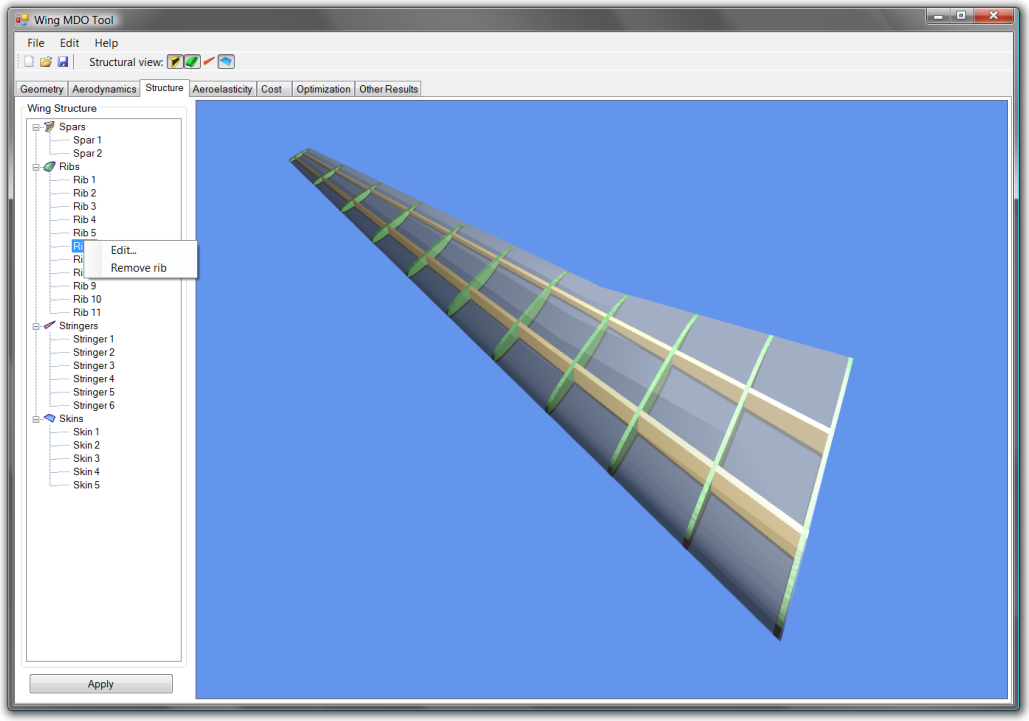


Figure 4.3: Structure screen

toggle on or off the visualization of the different types of elements.

The popup menus check the values of the user input and no changes are made unless they all fall within acceptable values (for instance, dimensions are required to be positive, real numbers).

The next tab controls *Awing*'s operation with options for boundary conditions. It employs the loading calculated in the aerodynamics section through *Zephyr* in order

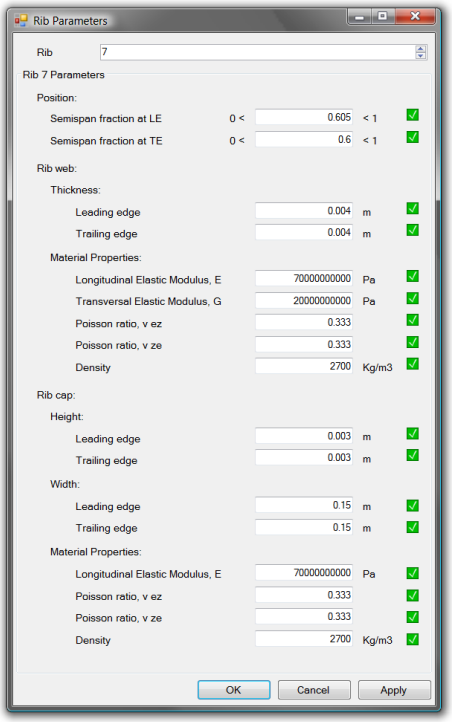


Figure 4.4: Ribs popup menu

to compute the respective static deformation. The user may then choose to view an animated plot of one of the first six vibration modes.

Other on screen information includes the estimated weight of the structure, the maximum static deformation for the current loading case and the values for the first six natural frequencies.

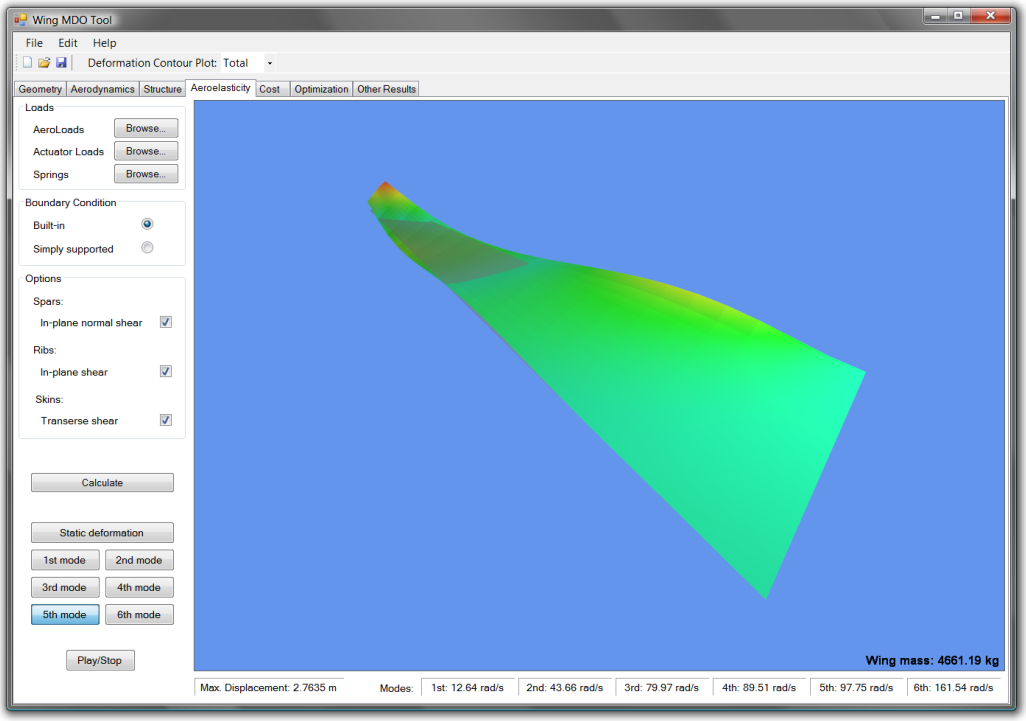


Figure 4.5: Aeroelasticity screen

Even though the application also serves as an analysis tool, it is the optimization tab that justifies its existence (Figure 4.6). The optimization options in this tab may be accessed after all the fields in the geometry and structure tabs (which define the baseline design and thus the starting point for the optimization procedure) have been filled in. By using the values that each of the variables takes for the baseline design as a reference, the user is asked to input the range for which an optimal value will be sought after. Structural variables are given ranges in terms of percentages in order to reduce user inputs to a minimum (e.g.: only one setting for the range of the web thickness of all spars).

The maximum and minimum values for a given variable are updated as the user

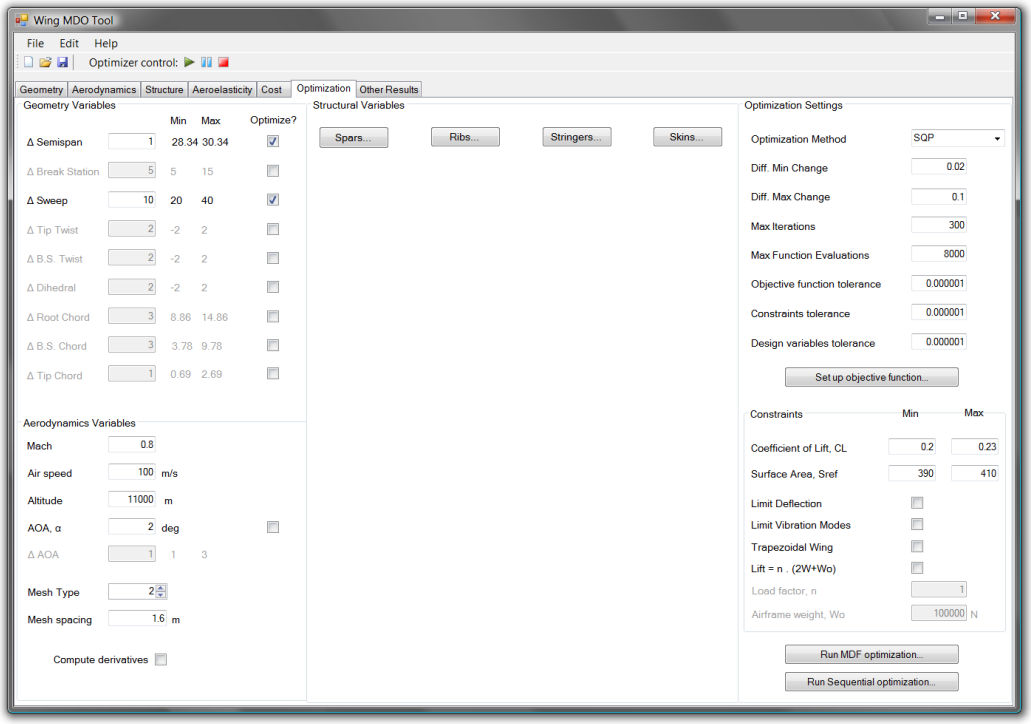


Figure 4.6: Optimization screen

fills in the respective Δ<variable name> field. Also, this section is provided with its own *Flight Conditions* group box so that the standalone aerodynamics module need not be used.

Finally, the optimization settings that mimic those available for the `fmincon` function (finite differencing settings, objective function, constraints and convergence tolerances) may be configured on the group box to the right, with the constraints for the physical problem (e.g.: $S_{ref}$, $C_L$) being defined below.

The final screen serves as a repository for additional information concerning the current design such as the listing and decomposition of the force totals in vehicle and wind axes, value of $\frac{L}{D}$, aspect ratio ($A$) and computed flutter speed, among others.

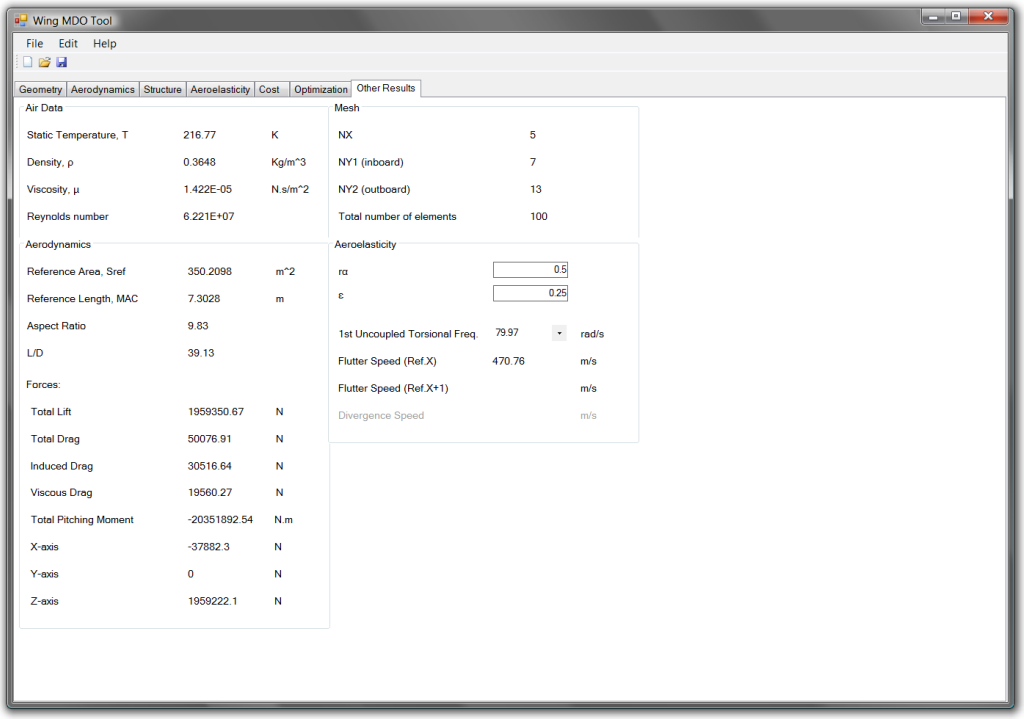


Figure 4.7: Other results screen

Owing to the modular nature of the interface and its intrinsic advanced graphics capabilities, it is also suited to serve as a docking point for future, higher-fidelity modules. Also, by designing the application to be more intuitive and by giving the user direct control over all the variables in play, the task of obtaining relevant results may be accomplished much faster even for someone unfamiliar with the program.

# Chapter 5

# Wing Design Optimization

In this chapter, the interactions between the modules are detailed, as is their linkage with the system level optimizer. Before presenting any meaningful optimization results though, the choice of design variables and the basis for the selection of constraints and objective function needs to be justified.

## 5.1 Formulation of the MDO problem

A typical engineering optimization problem is defined as the minimization of some objective function $f(\mathbf{x})$ ($\mathbf{x}$ being the vector of design variables, discussed in Sec. 5.1.1). In this case, where there are both equality and inequality constraints involved, the problem may be defined as ([41]):

$$\texttt{Minimize}: \qquad f(\mathbf{x}) \tag{5.1}$$

$$\texttt{subject to}: \quad \mathbf{A_{equality}}.\mathbf{x} = \mathbf{b_{equality}} \tag{5.2}$$

$$\mathbf{c_{equality}}\left(\mathbf{x}\right) = 0 \tag{5.3}$$

$$\mathbf{A}.\mathbf{x} \leq \mathbf{b} \tag{5.4}$$

$$\mathbf{c}\left(\mathbf{x}\right) \leq 0 \tag{5.5}$$

$$\mathbf{LB} \leq \mathbf{x} \leq \mathbf{UB} \tag{5.6}$$

Eqs. 5.2 and 5.3 refer to the linear and nonlinear equality constraints, respectively, whereas Eqs. 5.4 and 5.5 are the linear and nonlinear inequality constraints, in that order. Eq. 5.6 establishes the lower and upper bounds for the design variables.

### 5.1.1 Design variables

Most of the design variables available for optimization have already been hinted at the previous two chapters, when parameterizing both the geometry and the internal structure of the wing. Nevertheless, tables 5.1 and 5.2 are presented in order to summarize all that information:

Table 5.1: List of design variables (aerodynamics and geometry)

| **Design variable** | **Units** | **No. of instances** | **Obs.** |
|---|---|---|---|
| AOA, $\alpha$ | [deg] | 1 | readily converted to rad |
| Semispan, $\frac{b}{2}$ | [m] | 1 | |
| Break station, $bs$ | [m] | 1 | |
| LE Sweep, $\Lambda_{LE}$ | [deg] | 1 | |
| Tip twist | [deg] | 1 | |
| Break station twist | [deg] | 1 | |
| Dihedral, $\varphi$ | [deg] | 1 | |
| Root chord, $c_r$ | [m] | 1 | |
| Break station chord, $c_{bs}$ | [m] | 1 | |
| Tip chord, $c_t$ | [m] | 1 | |

Table 5.2: List of design variables (structure)

| **Design variable** | **Units** | **No. of instances** | **Obs.** |
|---|---|---|---|
| root position | | no. of spars | as fraction of $c_r$ |
| tip position | | no. of spars | as fraction of $c_t$ |
| web thickness at root | [m] | no. of spars | |
| web thickness at tip | [m] | no. of spars | |
| cap height at root | [m] | no. of spars | |
| cap height at tip | [m] | no. of spars | |
| cap width at root | [m] | no. of spars | |
| cap width at tip | [m] | no. of spars | |
| LE position | | no. of ribs | as fraction of $\frac{b}{2}$ |
| TE position | | no. of ribs | as fraction of $\frac{b}{2}$ |
| web thickness at LE | [m] | no. of ribs | |
| web thickness at TE | [m] | no. of ribs | |
| cap height at LE | [m] | no. of ribs | |
| cap height at TE | [m] | no. of ribs | |
| cap width at LE | [m] | no. of ribs | |
| cap width at TE | [m] | no. of ribs | |
| root position | | no. of stringers | as fraction of $c_r$ |
| tip position | | no. of stringers | as fraction of $c_t$ |
| height at root | [m] | no. of stringers | |
| height at tip | [m] | no. of stringers | |
| width at root | [m] | no. of stringers | |
| width at tip | [m] | no. of stringers | |
| thickness | [m] | no. of skins | |
| thickness ratio | | no. of skins | between tip and root |

Along with the variables previously introduced in each of the two analyzer modules, the angle of attack is now also considered as a variable, rather than simply a flight condition parameter as suggested in Chapter 2. This is because in order to obey some of the nonlinear constraints which can be imposed upon the system (e.g.,

$C_L$, $L = n\,W$. See (Sec. 5.1.3)), this additional degree of freedom may be required to avoid over constraining the problem and eliminating all feasible solutions.

The maximum number of variables that may be selected for an optimization run is dependent on the limits of the structural solver (see Sec. 3.2). Given the information on tables 5.1 and 5.2, the maximum number of design variables that can be accommodated for a given baseline design is:

$$\begin{aligned} Max.no.of design variables &= 4 + \\ &\quad + No.of spars \times 8 + \\ &\quad + No.of ribs \times 8 + \\ &\quad + No.of stringers \times 6 + \\ &\quad + No.of skin panels \times 2 \end{aligned} \tag{5.7}$$

The value of 4 corresponds to the angle of attack plus the geometric variables that do not have to do with quantities evaluated at the break station nor twists or dihedral angles. This due to the fact that the structural solver will only accept untwisted trapezoidal wings with no dihedral (Sec. 3.2). The total gives an absolute maximum of 314 design variables, if both the aerodynamics and structural solvers are used at their full capacity.

Because the design variables in play are likely to have values that differ by several orders of magnitude, they should be scaled. To achieve this, a mapping is established for each variable chosen for optimization, so that the optimizer will only be assigning them values within the interval $[-1, 1]$. This mapping is based, of course, on the lower and upper bounds for the actual values of the design variables (for variable $i$):

$$x_i = y_i \left( \frac{upper_i - lower_i}{2} \right) + baseline_i \tag{5.8}$$

where $y_i \in [-1, 1]$. In an effort to reduce the workload during the definition of the lower and upper bounds for each variable, the maximum deviation from the baseline design ($\Delta_i$) is used instead. This effectively cuts down the amount of required inputs by half. Then:

$$x_i = baseline_i + y_i \, \Delta_i \tag{5.9}$$

Special cases exist where a value for $\Delta_i$ is specified such that the lower bound would be negative, when that would not have any physical meaning (e.g. all linear dimensions). In those situations, the lower bound is forcibly set to zero by using $\Delta_i$ as a pseudo-baseline value:

$$x_i = \Delta_i + y_i \, \Delta_i \tag{5.10}$$

In these cases the mapped value for $baseline_i \rightarrow y_i(baseline_i)$, will no longer be zero as it usually would, but higher.

### 5.1.2 Dynamic linear constraints

The linear constraints are mostly to keep the design physically feasible, i.e., preventing spars, ribs and stringers from overlapping, as well as keeping the semispan larger than the location of the breakstation. Also, the position of the structural elements should not exceed the limits of the planform and therefore all chord and semispan fractions are limited between 0 and 1. Because of the versatile nature of the combination of interface and optimizer, these constraints need to be heuristically created.

A certain structural element has to be constrained by the ones adjacent to it (as seen on Figures 5.1 and 5.2). This is why the array containing the data pertaining to

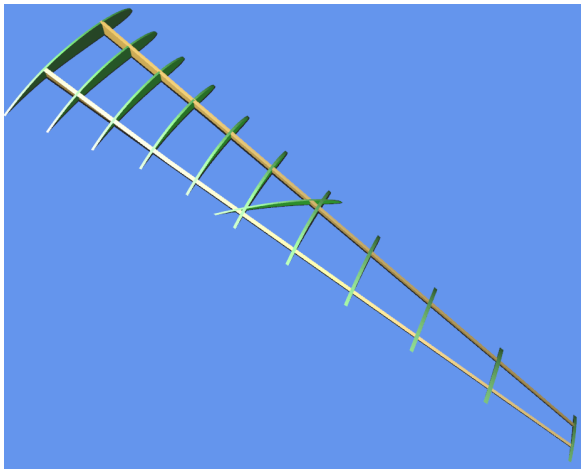

Figure 5.1: Improperly constrained rib

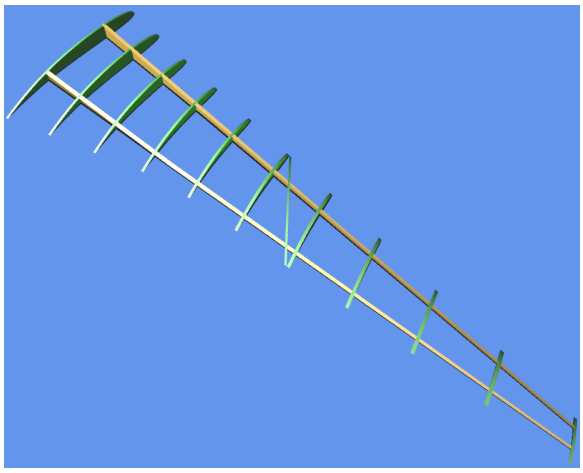

Figure 5.2: Properly constrained rib

each structural element needs to be sorted in a way that geometrically adjacent elements are also adjacent in terms of indexing (indexing criterion is root chord fraction or LE semispan fraction, whichever is applicable). The procedure to enforce these constraints is straightforward but tedious, especially since the parameters in question

may be either fixed or considered as design variables. Both equality and inequality linear constraints are specified as a linear system of equations/inequalities (Eqs. (5.2) and (5.4)) in which each line has to be reworked should one variable become fixed:

1)If the constraint involved only one former variable, that line is simply removed;

2)If the constraint includes variables other than the one being fixed, the latter's value is moved to the right side of the equation/inequality and subtracted to vector $\mathbf{b}$ or $\mathbf{b_{equality}}$, whatever the case (for all the case studies covered in this work, only linear inequalities were used).

To simplify the implementation of this dynamic creation of constraints, the second case only applies to the relation between semispan and break station location (when the wing is not constrained to have a trapezoidal planform as seen on Sec. 5.1.1), since all the variables concerning the placement of a certain type of structural elements are enabled or disabled through a single switch. Therefore, all relationships between them disappear simultaneously from the set of linear constraints (e.g., all leading edge positions of ribs becoming fixed parameters). Underlaying all of this is of course the need to also embed the mappings of the design variables (Eqs. (5.9) and (5.10)) into Eqs. (5.2) and (5.4).

### 5.1.3 Nonlinear constraints

Nonlinear constraints are usually based on the results of the analyzer modules, though they might also result from the nonlinear combination of two or more design variables. The application developed allows virtually any of the outputs from either analyses or a combination thereof to be used as a nonlinear constraint. Though in the current version only a handful of these saw actual implementation in the user interface (Chapter 4), others may be easily accessed through the source code.

The nonlinear constraints also come in terms of equalities or inequalities (Eqs. (5.3) and (5.5)), but in this case the RHS is always zero. Some examples of nonlinear constraints that are applicable to this type of problem (aerostructural optimization) are presented in Table 5.3:

Table 5.3: Examples of nonlinear constraints

| **Constraint** | **Obs.** |
|---|---|
| $C_{L_{lb}} - C_L \leq 0$ | lower bound for design $C_L$ |
| $C_L - C_{L_{ub}} \leq 0$ | upper bound for design $C_L$ |
| $S_{ref_{lb}} - S_{ref} \leq 0$ | lower bound for planform reference area |
| $S_{ref} - S_{ref_{ub}} \leq 0$ | upper bound for planform reference area |
| $\omega_{i_{specified}} - \omega_i \leq 0$ | vibration mode constraint |
| $L - n(2W_{wing} + W_{other}) = 0$ [1] | maneuver at load factor $n$ (e.g. for cruise, $n = 1$) |

Table 5.4: Numerical implementation of nonlinear constraints exemplified in Table 5.3

| **Constraint** | **Obs.** |
|---|---|
| $C_{L_{lb}} - C_L \leq 0$ | lower bound for design $C_L$ |
| $C_L - C_{L_{ub}} \leq 0$ | upper bound for design $C_L$ |
| $\frac{S_{ref_{lb}}}{S_{ref}} - 1 \leq 0$ | lower bound for planform reference area |
| $\frac{S_{ref}}{S_{ref_{ub}}} - 1 \leq 0$ | upper bound for planform reference area |
| $\frac{\omega_{i_{specified}}}{\omega_i} - 1 \leq 0$ | vibration mode constraint |
| $\frac{L}{n(2W_{wing}+W_{other})} - 1 = 0$ [1] | maneuver at load factor $n$ (e.g. for cruise, $n = 1$) |

Because numerical methods used for optimization are not indifferent to the way the constraints are specified, these nonlinear constrains are actual implemented as in Table 5.4 (note that the coefficient of lift is already nondimensional and its order of magnitude is 1) [4]. In this way, all the output variables are nondimensional and

[1] $W_{other}$ means the weight of the whole vehicle, discounting the wing structure. For a real life scenario, this might constitute a preliminary estimate.

within the same order of magnitude, which will surely benefit numerical convergence by preventing some of the constraints from dominating the others. Care must be taken when employing these constraints, however, since if a point very close (less than the constraint tolerance specified - Sec. 5.2) to or within the feasible region of the design space is not supplied as a baseline, the method is unlikely to be successful and optimization is aborted.

### 5.1.4 Objective function

Objective, cost or merit functions are some of the various names for the same entity. The objective function can be classified as being single or multi-objective, depending on whether it is weighting one or multiple outputs simultaneously.

The current approach toward the definition of an objective function is twofold. The first is the classical weighted sum method. The second involves the definition of a single performance measure, which, in actuality, is an ensemble of several output variables but has physical meaning.

#### Weighted sum approach

The most common way of defining a function for minimization of several objectives is to form a weighted sum of them. More often than not, the choice of the weights is arbitrary and thus controversial, as it will have a significant impact on the results. These weights must, however, be corrected according to the magnitude of the various objectives involved. An example:

$$f(\mathbf{x}) = -K \frac{\frac{L}{D}}{\left(\frac{L}{D}\right)_{magnitude}} + (1-K) \frac{W}{W_{magnitude}} \tag{5.11}$$

In Eq. (5.11), $K$ represents a (positive) weighting factor so that the sum of all the weights adds up to 1. The first term is multiplied by -1 since we would be interested in maximizing the lift to drag ratio in this example. Though this gives this approach some structure, the choice of factor $K$ must still be justified, based on Pareto front plots, for instance.

#### Breguet range equation

To avoid the ambiguity of the choice of weights mentioned above, a single performance measure with a more practical meaning is also introduced. Hence, the ubiquitous Breguet range equation is taken as an example. It is defined as:

$$R = \frac{V_{cruise}}{g\,SFC}\frac{L}{D}\log\frac{W_i}{W_f} \tag{5.12}$$

where $V_{cruise}$ is the design cruise speed and $SFC$ stands for the Specific Fuel Consumption (units: $\mathrm{Kg.s^{-1}.N^{-1}}$) which depends solely on the propulsion system. $W_i$ and $W_f$ are the initial and final weights for the cruise flight phase, respectively. An objective function based on this equation dispenses with a weighted approach using output variables such as $\frac{L}{D}$ or $C_D$, for instance. The weighting between competing objectives is instead implicitly defined in a meaningful and physical manner.

## 5.2 Optimizer implementation

To expedite the development, the optimizer uses the capabilities of the MATLAB® *Optimization Toolbox*. This toolbox implements gradient based and non-gradient based methods for both medium and large scale problems. The non-gradient based methods are further complemented by the *Genetic Algorithm and Direct Search Tool-*

*box*, which, as the name implies, employs evolutionary algorithms. Evolutionary algorithms are particularly robust and can tackle functions where gradient based algorithms struggle to converge. Their main disadvantage is that they usually require a large number of function evaluations in order to obtain satisfactory results. The application of evolutionary algorithms to maximize wing efficiency through shape optimization was actually the main topic of papers by Kroo [42] and Gonzalez et al. [43].

The usage of the large scale algorithms implemented in the *Optimization Toolbox*, though certainly tempting (should a large number of design variables be chosen for optimization - Sec. 5.1.1), is precluded since the ones available are not able to take all types of constraints into consideration simultaneously. Therefore, a medium scale algorithm, SQP - *Sequential Quadratic Programming* - is used instead, as it allows the greatest versatility in defining the design optimization problems.

SQP methods have been thoroughly tested and are among the most capable gradient based methods, being credited with a high percentage of successful solutions. They have also seen some use in aerostructural optimization [28], [44]. These algorithms assume a second order approximation of the objective and constraints functions, therefore leading to a higher convergence rate when compared with their linear counterparts.

Being a gradient-based method, SQP requires information on the gradient of the objective function at each iteration. This means that, at each iteration, either the analyzer modules provide the gradients themselves, along with the value of the objective function, or the optimizer will be required to call the analyzers once for each design variable, in order to estimate the derivatives through finite-differencing. The latter approach had to be selected since access to the source code of the structural module was limited, effectively precluding the use of automatic differentiation. The future

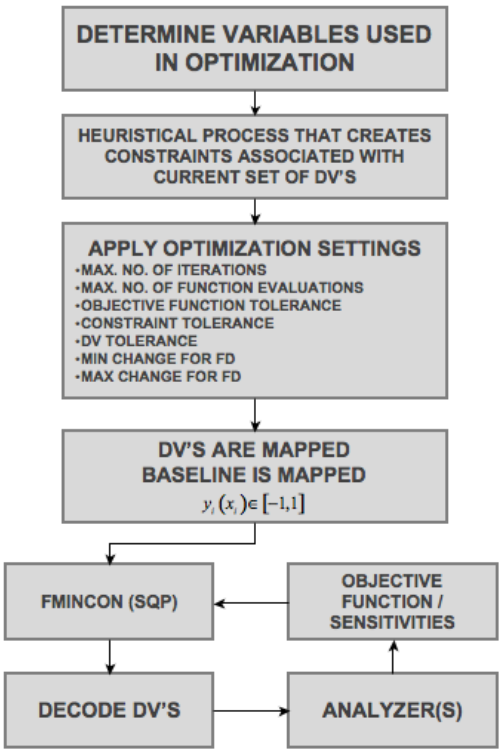


Figure 5.3: Optimizer flowchart

implementation of an automatic differentiation capability in the analyzer codes, by operator overloading in C++ and FORTRAN, for instance, would greatly increase the performance of the whole package. Figure 5.3 portrays the process in which the optimizer (using the `fmincon` function) is included.

This procedure makes it easier to integrate different instances of the optimizer, either it be implementing different methods or simply a revised version of the current one (provided they accept the same type of inputs).

Also evidenced in Figure 5.3 is the ability to customize the algorithm according to the settings available for the `fmincon` function. These include the stopping tolerances for changes in the value of either the objective function or the design variables,

the maximum allowable for constraint violation, the maximum number of function evaluations and iterations for the algorithm and finally, the minimum and maximum finite differencing step. The latter is a setting of paramount importance, as it has a big impact on the computation of sensitivities. Its value should be tuned for each specific problem, bearing in mind that it refers to the mapped values of the variables (Eqs. (5.9) and (5.10)). The values chosen should then be such that within its optimization range ($\Delta_i$), the minimum change in a certain DV will produce a measurable change in the objective function. Too great a value for the maximum change for finite differencing is not desirable either since the computed derivatives will then lack precision (truncation error vs. round off error).

## 5.3 MDO Strategies

The modules in an MDO framework may be arranged in several ways, more often than not due to performance concerns. MDO techniques may be classified as single or multilevel. Multilevel means that besides a system optimizer having control over general, system wide design variables, there are also disciplinary optimizers coupled with each of the analyzer modules, which exert a more local control over a subset of DV's. Also, some design variables, particularly the ones to which the disciplines are the most sensitive, might require more changing than others. The reason for doing this is that it is not unusual for one of the analyzer modules to be computationally more expensive than all the others, which means that steps should be taken in order to avoid the calls to that more expensive function. Also, other distinctions can be made with respect to whether the state variables (e.g. displacements) are recomputed at each iteration.

The following strategies that were implemented to date, are intended to function

as examples of the modularity of the framework developed.

### 5.3.1 MDF formulation

Among the various multidisciplinary design optimization techniques available, one that has seen much use is called MDF which stands for Multidiscipline Feasible (also called Single-NAND-NAND [28]). In this arrangement (Figure 5.4), the optimizer has control over all the design variables, feeding new values for the DV's directly to the analyzer modules, while receiving information on the respective values for the objective function and the sensitivities. The interaction between disciplines is, in

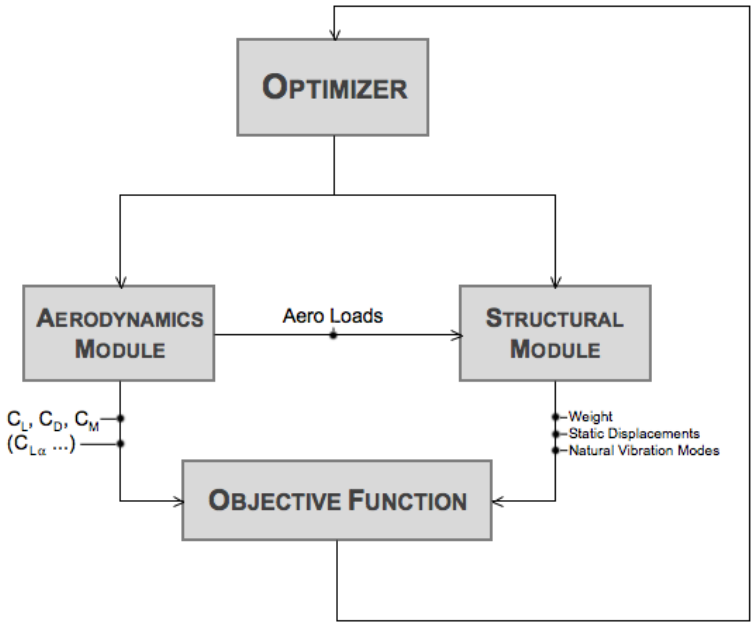


Figure 5.4: MDF strategy

the general case, a two-way track. Due to limitations in the implementation of both modules, however, there is no real fluid-structure interaction capability in the current

approach. This means there is no loop when computing an equilibrium between static displacements and aerodynamics load distribution, thus simplifying and reducing the computational cost of the problem at the expense of accuracy.

### 5.3.2 Sequential optimization

So as to compare the more common MDF to a multilevel approach, the following sequential arrangement was implemented (Figure 5.5). This type of approach is described in [45], [46] and [47].

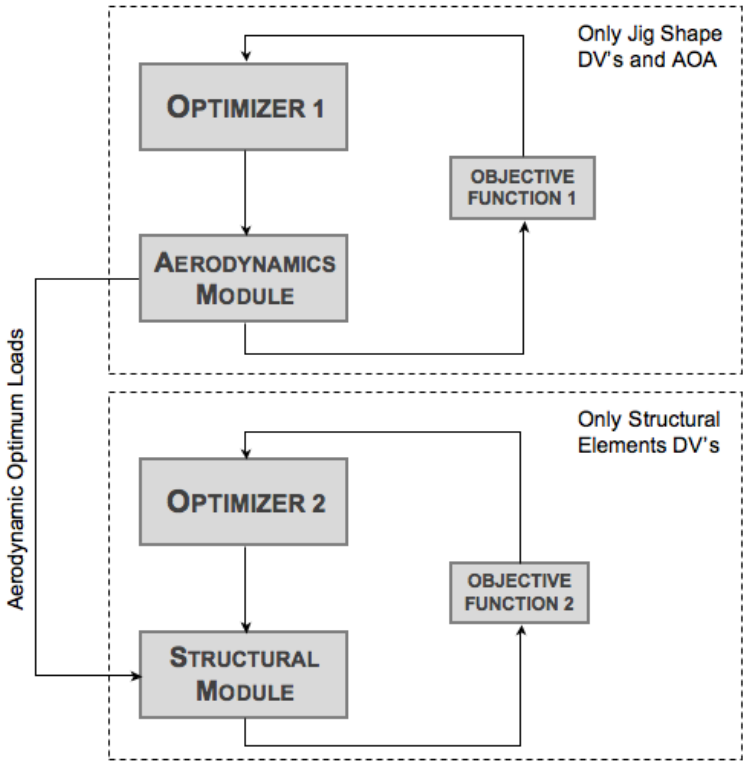


Figure 5.5: Sequential optimization strategy

This formulation effectively divides the problem into two distinct subproblems and

is not necessarily equivalent to MDF. There is no global optimizer, and the process is carried out only once (i.e., no aerodynamic re-optimization after the structural optimization). The process itself mimics the classical approach in aircraft design - aerodynamics then structures. Although the solution to this problem stated will generally be different than MDF, overall, the computational cost will be lower.

## 5.4 Case study 1 - Aerodynamic optimization

In this first case study, a problem of pure aerodynamic performance optimization will be solved. This will be done with both a single and multi-objective cost functions. For this wing design optimization problem, the planform of the Boeing 787 airliner (Figure 5.6) was chosen as the baseline configuration. Some of the baseline values


Figure 5.6: Boeing 787 *Dreamliner*, Boeing Co.©

for DV's are estimates (see Table 5.5), since most of the details are proprietary data

from Boeing [48], especially the airfoils. It is assumed that these are supercritical [1], since the aircraft is designed to cruise at transonic speeds, so a supercritical airfoil was chosen arbitrarily from [22] and used for all sections.

Table 5.5: Baseline configuration details for Case Study 1

| **Baseline dimensions** | **Value** | **Obs.** |
|---|---|---|
| Semispan, $\frac{b}{2}$ | 29.34 m | [49] |
| Break station, $bs$ | 11.60 m | [49] |
| LE Sweep, $\Lambda_{LE}$ | 30 deg | estimate |
| Tip twist | 0 deg | estimate |
| Break station twist | 0 deg | estimate |
| Dihedral, $\varphi$ | 5 deg | estimate |
| Root chord, $c_r$ | 11.86 m | estimate |
| Break station chord, $c_{bs}$ | 6.42 m | [49] |
| Tip chord, $c_t$ | 1.69 m | [49] |
| Airfoil | | |
|  | | |
| NASA/Langley Whitcomb integral supercritical airfoil | | |

### 5.4.1 Single Objective, Single Discipline

In this section, the baseline configuration detailed in Table 5.5 will be optimized according to a single performance criterion, $\frac{L}{D}$ - the lift to drag ratio. Hence:

$$f(\mathbf{x}) = -\frac{L}{D} \tag{5.13}$$

[1] Supercritical airfoils are designed to delay the appearance of areas of supersonic flow over a wing ($M_{crit}$) as this will also delay drag divergence (occurring at the drag divergence Mach number $M_{dd}$), a consequence of the sudden drag rise observed at transonic speeds when a zone of supersonic flow over an airfoil ends abruptly at a shockwave.

is the function to be minimized. The bounds and constraints chosen to be imposed are: Flight conditions are set to be $M_\infty = 0.8$, which means $V_\infty = 236.14$ m.s$^{-1}$@11000m.

Table 5.6: Bounds and constraints for Case Study 1: Single objective

| **Design variable** | **Minimum Value** | **Maximum Value** |
|---|---|---|
| Semispan, $\frac{b}{2}$ | 28.34 m | 30.34 m |
| Break station, $bs$ | 6.60 m | 16.60 m |
| LE Sweep, $\Lambda_{LE}$ | 20 deg | 40 deg |
| Tip twist | -2 deg | 2 deg |
| Break station twist | -2 deg | 2 deg |
| Root chord, $c_r$ | 8.86 m | 14.86 m |
| Break station chord, $c_{bs}$ | 3.42 m | 9.42 m |
| Tip chord, $c_t$ | 0.69 m | 2.69 m |
| $0.31 \leq C_L \leq 0.34$ | | |
| $340 \leq S_{ref} \leq 360$ | | |

The angle of attack is 0 deg and $Re_{trans} = 5 \times 10^5$.

Table 5.7 highlights the main performance gains from this purely aerodynamic optimization of the wing geometry. A view of the baseline and optimized configurations is presented in Figure 5.7, along with the convergence plot for the objective function (multiplied by a factor of -1). Though it is not guaranteed to be the global optimum, the final design was attained within a $1 \times 10^{-4}$ tolerance for change in the objective function.

Table 5.7: Comparison between baseline and optimized designs - Case study 1: Single objective

| **Design/Output variable** | **Baseline Value** | **Optimized Value** | **Difference** |
|---|---|---|---|
| Semispan, $\frac{b}{2}$ | 29.34 m | 30.34 m | +3.4% |
| Break station, $bs$ | 11.60 m | 16.32 m | +40.7% |
| LE Sweep, $\Lambda_{LE}$ | 30 deg | 40 deg | +33.3% |
| Tip twist | 0 deg | -2 deg | - |
| Break station twist | 0 deg | -1.2 deg | - |
| Root chord, $c_r$ | 11.86 m | 12.41 m | +4.6% |
| Break station chord, $c_{bs}$ | 6.42 m | 4.52 m | -29.6% |
| Tip chord, $c_t$ | 1.69 m | 0.72 m | -57.4% |
| $C_L$ | 0.3215 | 0.3400 | +5.8% |
| $C_{D_i}$ | 0.0029 | 0.0023 | -20.7% |
| $C_{D_f}$ | 0.0055 | 0.0056 | +1.8% |
| $C_D$ | 0.0055 | 0.0056 | +1.8% |
| $S_{ref}$ | 355.9 $m^2$ | 349.9 $m^2$ | -1.7% |
| $L$ | $1.164 \times 10^6$ N | $1.210 \times 10^6$ N | +4.0% |
| $D$ | $3.027 \times 10^4$ N | $2.796 \times 10^4$ N | -7.6% |
| $\frac{L}{D}$ | 38.45 | 43.29 | +12.6% |

The improvement in the lift over drag ratio was 12.6%, mainly due to a significant decrease in the induced drag, at the cost of a slight increase in friction drag. We must be reminded, though, that this is a purely aerodynamic optimization with no concern whatsoever for the behavior of the structure itself. A greater aspect ratio, no matter how beneficial in terms of performance, will always conflict with strength requirements, as we shall see in the subsequent sections. It can be observed in Figure 5.7, that in one of the earlier iterations a design which outperforms the final one is attained. This occurs at the expense of a violation in the constraints for $C_L$ and $S_{ref}$ which turns out to be surpass the respective tolerance.

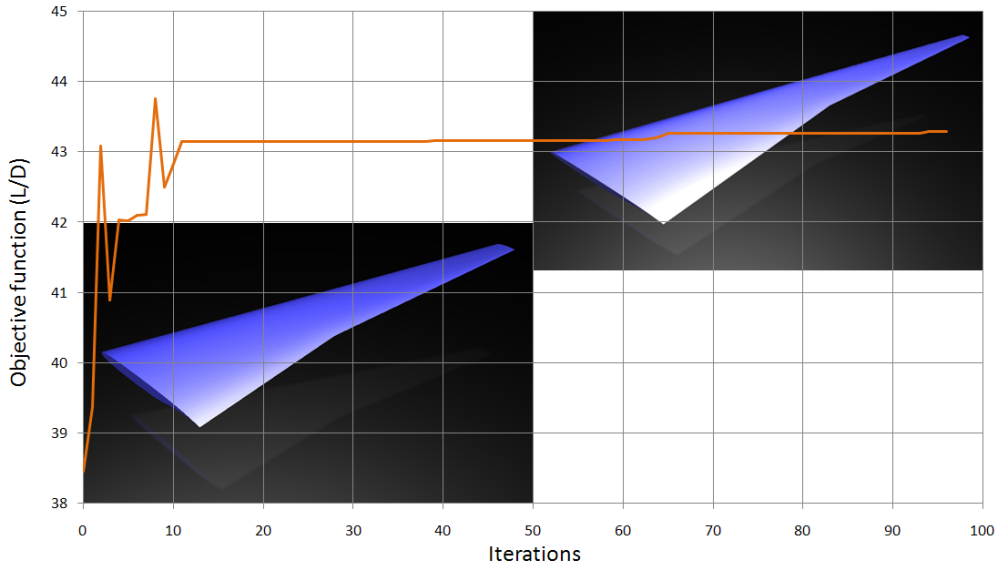


Figure 5.7: Objective function convergence plot with baseline and optimized designs in the background

### 5.4.2 Multiobjective, Single Discipline

For the multiobjective optimization problem, the same planform will be used, albeit with no dihedral ($\varphi$) and a different airfoil section, a symmetrical one (NACA0009 - 9% thickness ratio), in order to expedite the computations. This is beneficial since now we are aiming at plotting the Pareto front for the multiobjective problem and as such several distinct optimization runs will be required. Also, the twists were removed from the design variable set and the bounds and constraints for the design variables were readjusted:

The constraint for $C_L$ was relieved since in this case we will be employing a cost function of the form:

$$f(\mathbf{x}) = 10\left(-K\ C_L + 100(1-K)\ C_D\right) \tag{5.14}$$

Table 5.8: Bounds and constraints for Case Study 1: Multi objective

| **Design variable** | **Minimum Value** | **Maximum Value** |
|---|---|---|
| Semispan, $\frac{b}{2}$ | 28.34 m | 30.34 m |
| Break station, $bs$ | 6.60 m | 16.60 m |
| LE Sweep, $\Lambda_{LE}$ | 20 deg | 40 deg |
| Root chord, $c_r$ | 8.86 m | 14.86 m |
| Break station chord, $c_{bs}$ | 3.42 m | 9.42 m |
| Tip chord, $c_t$ | 0.69 m | 2.69 m |
| $0 \leq C_L \leq 2$ | | |
| $340 \leq S_{ref} \leq 360$ | | |

The factor of 100 multiplying $C_D$ is to account for the expected magnitude of that quantity, whereas the inclusion of the overall factor of 10 was observed to lead to better numerical results. The values of $K$ range from 0 to 1 in order to cover an array of possibilities for the definition of the objective function.

Flight conditions are the same as in the previous case except for the angle of attack, which is now set at 2 deg. The results obtained while varying the value of $K$ in the aforementioned interval are plotted in Figure 5.8 to determine an approximation of the Pareto front.

Designs which are the most efficient in terms of the combination of $C_L$ and $C_D$ should be at the Pareto front. It is also immediately apparent that the baseline design is no such point, resting well within the feasible zone. Also worthy of note is the fact that an optimization run to find the maximum lift to drag ratio produced a point closer to the $C_L$ dominated area of the Pareto front. Though likely to occur in optimization scenarios where the ratio $\frac{L}{D}$ is high, this situation cannot be generalized. It is actually reasonable to assume that the lower the aspect ratio (and, by extension $\frac{L}{D}$), the further away from the $C_L$ dominated area of the Pareto front will the optimized maximum $\frac{L}{D}$ point move.

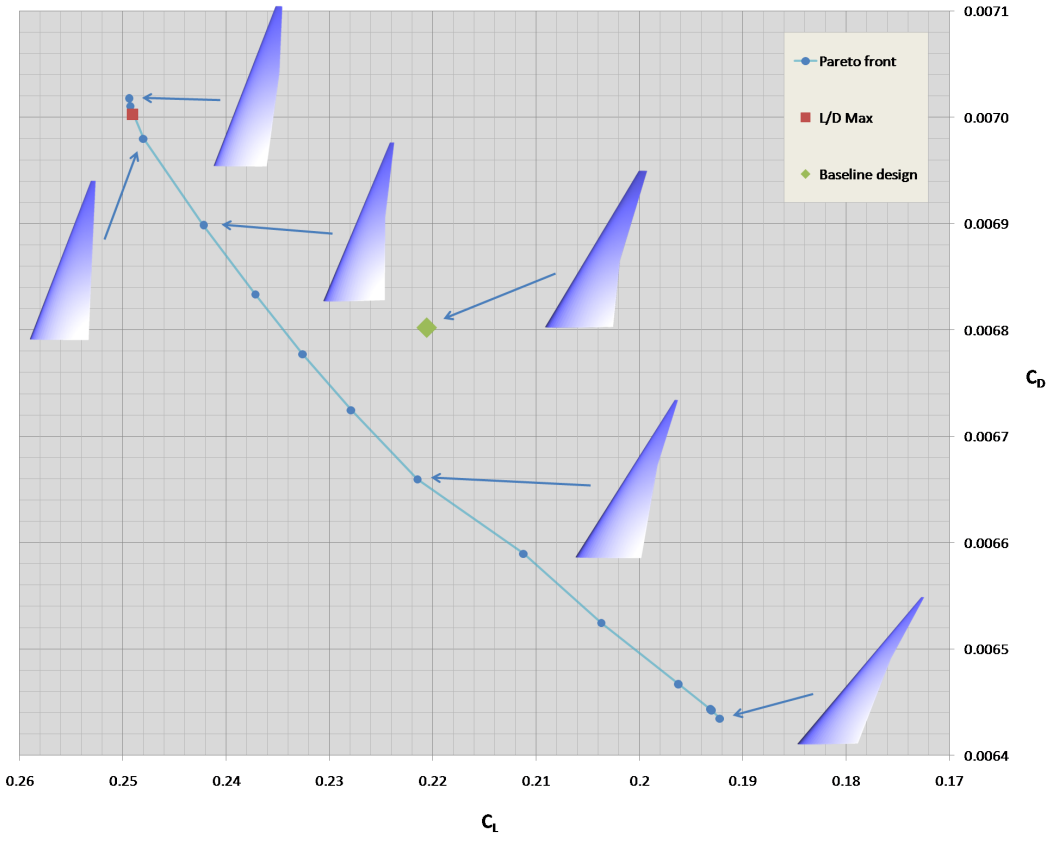


Figure 5.8: Pareto front and optimized designs for the Case 1 multiobjective problem

## 5.5 Case study 2 - Structural optimization

In this second single discipline optimization set-up, the structural module will be given emphasis by allowing the analysis of different arrangements for the structural components in the wing. The outer mold line of the wing will remain untouched, as that would change the distribution of the aerodynamic loads and therefore it would be required to run the aerodynamics module (effectively making it a multidisciplinary problem).

The baseline structure as shown in Figure 5.9 (which, due to the lack of detailed data on actual aircraft wings is but an estimate), is composed of 2 spars, 11 ribs, 12 stringers (6 pairs) and 10 skin panels (5 pairs), their dimensions being defined in Table 5.9. Since the current version of the structural module does not support non-trapezoidal wings, the planform used in Sec. 5.4.2 is corrected to become trapezoidal by adjusting the break station chord to 6.775 m. All structural elements are made of aluminum, except the skin, which is composed of carbon fiber composite, whose properties are defined in Appendix C. This brings the total mass to 4637.6 Kg (for one wing).

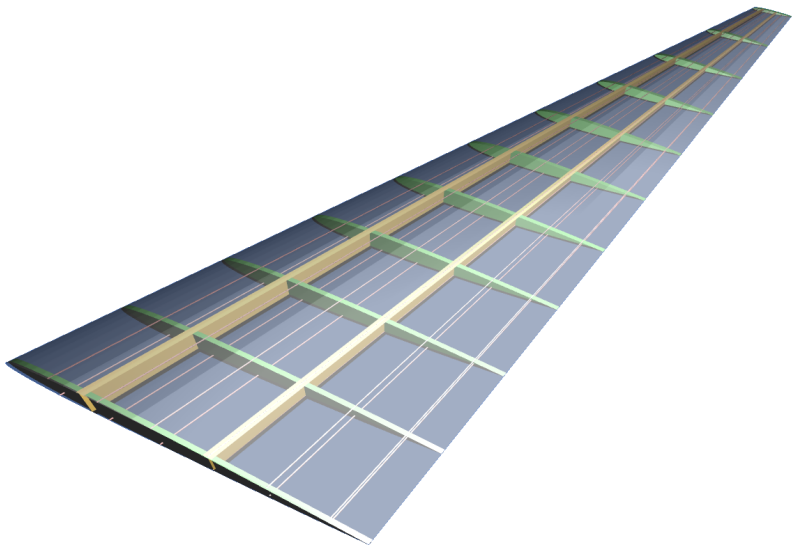

Figure 5.9: Baseline wing structure

To ensure a purely structural optimization[1], no external geometry parameters will be chosen as design variables. For this example, the variables and constraints in

[1]Nevertheless, since *Awing* needs a loading condition as input, an initial run of the aerodynamics module is required, using the same flight conditions as in Sec. 5.4.2

Table 5.9: Baseline structure - Case Study 2

| **Structural parameter** | **Baseline value** | **Obs.** |
|---|---|---|
| Spar root position | 0.25/0.6 | as fraction of $c_r$ |
| Spar tip position | 0.25/0.6 | as fraction of $c_t$ |
| Spar web thickness at root | 0.0060 m | |
| Spar web thickness at tip | 0.0050 m | |
| Spar cap height at root | 0.010 m | |
| Spar cap height at tip | 0.00500 m | |
| Spar cap width at root | 0.3000 m | |
| Spar cap width at tip | 0.1000 m | |
| Rib LE position | 0.005/0.105/0.205/0.305 0.405/0.505/0.605/0.705 0.805/0.905/1.000 | as fraction of $\frac{b}{2}$ |
| Rib TE position | 0.000/0.100/0.200/0.300 0.400/0.500/0.600/0.700 0.800/0.900/1.000 | as fraction of $\frac{b}{2}$ |
| Rib web thickness at LE | 0.0040 m | |
| Rib web thickness at TE | 0.0040 m | |
| Rib cap height at LE | 0.0030 m | |
| Rib cap height at TE | 0.0030 m | |
| Rib cap width at LE | 0.1500 m | |
| Rib cap width at TE | 0.1500 m | |
| Stringer root position | 0.15/0.30/0.45/0.60/0.75/0.90 | as fraction of $c_r$ |
| Stringer tip position | 0.15/0.30/0.45/0.60/0.75/0.90 | as fraction of $c_t$ |
| Stringer height at root | 0.0200 m | |
| Stringer height at tip | 0.0200 m | |
| Stringer width at root | 0.0200 m | |
| Stringer width at tip | 0.0200 m | |
| Skin thickness | 0.0050 m | |
| Skin thickness ratio | 1.0 | from root to tip |

Table 5.10 are driving the optimization.

Table 5.10: Bounds and constraints for Case study 2

| **Design variable** | **Minimum Value** | **Maximum Value** |
|---|---|---|
| Spar cap height at root | 0.0040 m (-60%) | 0.0160 m (+60%) |
| Spar cap height at tip | 0.0020 m (-60%) | 0.0080 m (+60%) |
| Rib semispan fraction at LE | baseline - 0.1 [1] | baseline + 0.1 [2] |
| Rib semispan fraction at TE | baseline - 0.1 [1] | baseline + 0.1 [2] |
| $\frac{0.90\,\omega_{i_{baseline}}}{\omega_i} - 1 \leq 0,\ i = 1, 2, 3$ | | |
| $\frac{\delta_{tip}}{0.075\frac{b}{2}} - 1 \leq 0$ | | |

The total number of design variables is then 26 - 4 related to spars and 22 related to ribs.

It is important to note that, in order to maintain a certain level of structural stiffness the maximum displacement at the tip was constrained when the wing is subject to the computed load (to 7.5% of the semispan), and so were the first three natural vibration frequencies in a way that they cannot drop below 90% of their respective baseline values. Though it would preferable to also have some sort of constraint on the structural safety factor, this cannot be for reasons that were explained at the beginning of Chapter 3. Additionaly, the ribs are constrained in the way explained in Sec. 5.1.2.

For this optimization run, the objective function will be simply defined as:

$$f(\mathbf{x}) = W \tag{5.15}$$

[1] If the lower bound becomes negative, it is set to 0.
[2] If the upper bound becomes greater than 1, it is set to 1.

so that the mass of the structure will be minimized (applies to starboard wing).

The results are presented in Table 5.11 and Figure 5.10. From inspection of Ta-

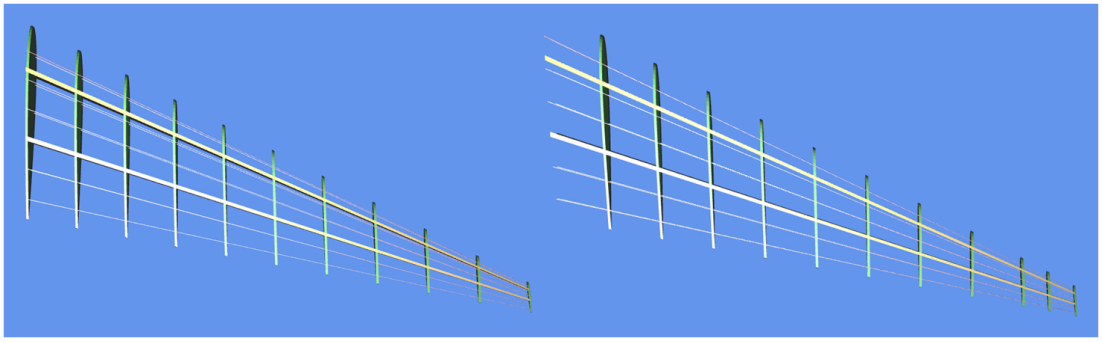

Figure 5.10: Baseline wing vs. weight optimized wing

ble 5.11, it is clear that the constraints established are preventing further optimization of the structure. Furthermore, the stiffness threshold based on the tip displacement is still far from being attained ($0.075 \times 29.34$ m $= 2.201$ m) and there was even a marginal increase in the constrained natural vibration frequencies. More importantly, there was a relevant change in structural weight which was the objective.

Table 5.11: Comparison between baseline and optimized designs - Case Study 2

| **Design/Output variable** | **Baseline Value** | **Optimized Value** | **Difference** |
|---|---|---|---|
| Spar 1 cap height at root | 0.0100 m | 0.0040 m | -60% |
| Spar 1 cap height at tip | 0.0050 m | 0.0020 m | -60% |
| Spar 2 cap height at root | 0.0100 m | 0.0040 m | -60% |
| Spar 2 cap height at tip | 0.0050 m | 0.0020 m | -60% |
| Ribs semispan fraction at LE | 0.005/0.105/0.205/ 0.305/0.405/0.505/ 0.605/0.705/0.805/ 0.905/1.000 | 0.105/0.205/0.305/ 0.405/0.505/0.605/ 0.705/0.805/0.900/ 0.950/1.000 | |
| Ribs semispan fraction at TE | 0.000/0.100/0.200/ 0.300/0.400/0.500/ 0.600/0.700/0.800/ 0.900/1.000 | 0.100/0.200/0.300/ 0.400/0.500/0.600/ 0.700/0.800/0.900/ 0.950/1.000 | |
| $W$ | $4.548\times10^4$ N | $4.239\times10^4$ N | -6.8% |
| $\omega_1$ | 11.20 rad.s$^{-1}$ | 11.22 rad.s$^{-1}$ | +0.2% |
| $\omega_2$ | 39.03 rad.s$^{-1}$ | 39.22 rad.s$^{-1}$ | +0.5% |
| $\omega_3$ | 88.56 rad.s$^{-1}$ | 89.27 rad.s$^{-1}$ | +0.8% |
| $\delta_{tip}$ | 1.585 m | 1.656 m | +4.5% |

## 5.6 Case study 3 - Aero-structural optimization

Finally, using the same baseline wing as in the previous case study, an aero-structural optimization, employing all types of design variables, was performed. The two distinct MDO strategies discussed in Sec. 5.3.1 and Sec. 5.3.2 are then compared.

The set of design variables chosen for this case is presented in Table 5.12.

Again, the wing is also constrained to present a simply trapezoidal planform and, in addition to the above, the spars are again linearly constrained as specified in Sec. 5.1.2.

Table 5.12: Bounds and constraints for Case study 3

| **Design variable** | **Minimum Value** | **Maximum Value** |
|---|---|---|
| AOA, $\alpha$ | 0 | 4 |
| Semispan, $\frac{b}{2}$ | 28.34 m | 30.34 m |
| LE Sweep, $\Lambda_{LE}$ | 15 deg | 45 deg |
| Spar chord fraction at root | baseline - 0.2 [1] | baseline + 0.2 [2] |
| Spar chord fraction at tip | baseline - 0.2 [1] | baseline + 0.2 [2] |
| Rib web thickness at LE | 0.0012 m (-70%) | 0.0068 m (+70%) |
| Rib web thickness at TE | 0.0012 m (-70%) | 0.0068 m (+70%) |
| Skin thickness | 0.0015 m (-70%) | 0.0085 m (+70%) |

$$0.2 \leq C_L \leq 0.23$$
$$390 \leq S_{ref} \leq 410$$
$$\frac{0.90\,\omega_{i_{baseline}}}{\omega_i} - 1 \leq 0,\ i = 1, 2, 3$$
$$\frac{\delta_{tip}}{0.075\frac{b}{2}} - 1 \leq 0$$

The objective function is defined as:

$$f(\mathbf{x}) = -K\frac{L}{D} + (1-K)\frac{W}{100} \tag{5.16}$$

where $\frac{L}{D}$ is the lift to drag ratio and $W$ is the mass of the wing (starboard side), measured in Kg. This objective function, however, only applies to the MDF formulation since for Sequential optimization it has to be partitioned in two: first $f(\mathbf{x}) = -\frac{L}{D}$ for the aerodynamics subproblem, followed by simply $f(\mathbf{x}) = W$ for the structural subproblem. The results obtained are compared in Figure 5.11 for several values of $K$. Flight conditions are as before (Case study 2) except for the angle of attack which is now a design variable.

[1] If the lower bound becomes negative, it is set to 0.
[2] If the upper bound becomes greater than 1, it is set to 1.

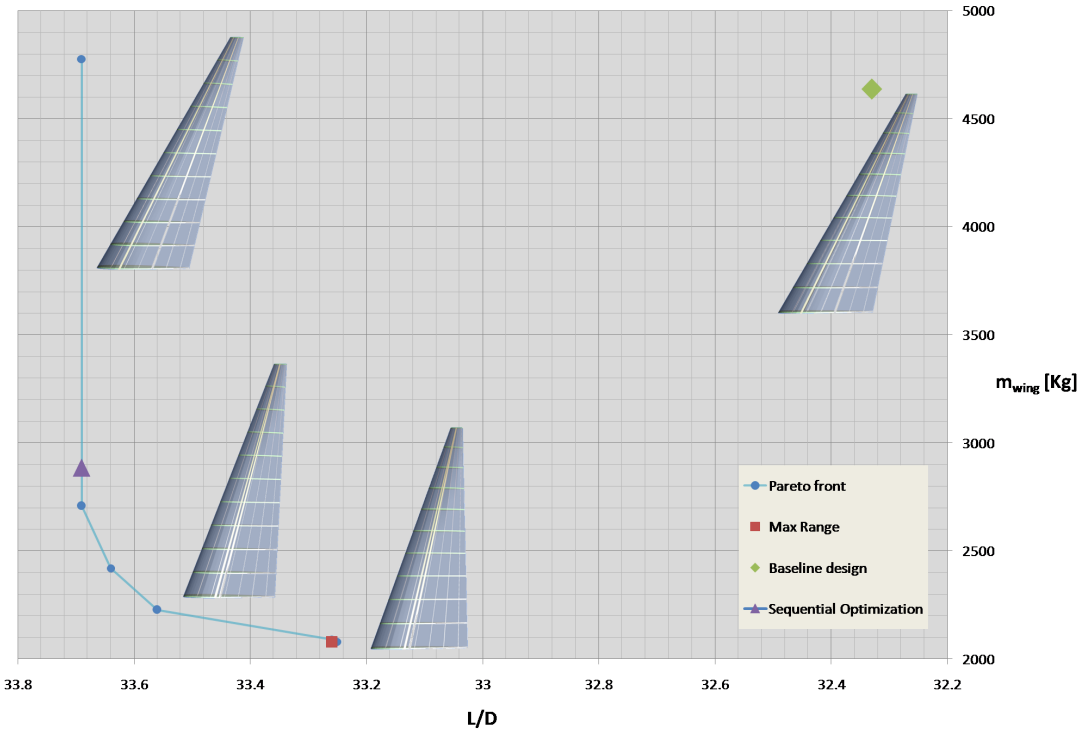


Figure 5.11: Pareto front for Case Study 3

Moreover, a single run of MDF based on the Breguet range equation is also displayed to again prove that such an objective function will also lead to a $p$-optimal design point. The range equation in this case was defined with the following values:

$$R = \frac{V_\infty}{9.80665 \times 20 \times 10^{-6}} \frac{L}{1.2D} \log\left(\frac{2W_{Wing} + 16W_{Wing} + 10000}{2W_{Wing} + 16W_{Wing}}\right) \tag{5.17}$$

Contrasting with Eq. 5.12, one may easily find that $g = 9.80665$ m.s$^{-2}$, $SFC = 20 \times 10^{-6}$ Kg.N$^{-1}$.s$^{-1}$ [50] were the values used. The 20% increase in drag in the $\frac{L}{D}$ ratio is to account for the drag of the rest of the aircraft, which in turn is considered not to produce any appreciable lifting force. On another note, the values for the

initial and final weights accomodate a 10000 Kg total fuel consumption, while also assuming the empty weight plus non-deployable payload to be 18 times the weight of a single wing. The optimized design presented in the Pareto front plot of Figure 5.11 represents a 115% increase in range over the baseline design (7894 Km vs. 3668 Km). This apparently surreal figure is of course explained through the fact that the baseline wing was made up somewhat arbitrarily, strictly for academic purposes due to the lack of data on real wing structures. A real world scenario would certainly yield a substantially lower improvement.

Regarding the Sequential Optimization strategy, the constraints imposed on the structure (displacements, natural vibration modes - referred to the baseline wing) are only applied on the second subproblem since there is no way to verify them in the first part of the optimization (dominated by the aerodynamics solver). This explains in part why the result for Sequential Optimization dominates some of the points obtained for the MDF problem. In addition, the constraints of the problem work in a way so that the maximum value of $\frac{L}{D}$ attainable is 33.69, which also explains the straight line in the Pareto front (which is then actually a constraint) even as the value of $K$ in Eq. 5.16 increases.

In terms of computational cost, it was found that though the Sequential Optimization implementation was faster than MDF, this was only by a small margin since a single optimization run might take up to 12 hours (with the proposed number of DV's) and is completely dominated by the structural module (which is the one that is called more often in SO due to the number of structural DV's). This is mainly because every call to the structural module takes between 20 and 30 seconds (depending on the complexity of the wing structure, i.e., number of components) and the sensitivities are evaluated independently.

# Chapter 6

# Conclusions

First and foremost, as is, the tool has been proven to allow the optimization of wing designs with respect to a set of around 40 variables. Notwithstanding, several shortcomings are recognized in the current implementation. Though more design variables could be chosen for optimization, the practicality of the application quickly diminishes since the optimizer employs a gradient based method and sensitivities are obtained through additional function evaluations. This requires additional computation time which rises quickly as the number of DV's increases. The future implementation of an adjoint or automatic differencing method for the analyzer modules would greatly help in ameliorating this issue. In order to increase the number of variables beyond the above mentioned figure and keep the problems tractable, large-scale, direct search methods could be employed. Alternatively, a hybrid approach using both one of these methods to narrow down the search area, followed by a gradient based method, could be used instead.

An apparent limitation of the MCR precludes the simultaneous existence of two distinct instances of the optimizer, which in turn prevents the immediate implementation of MDO strategies such as Collaborative Optimization, among others. One

of the priorities of future work on this tool will therefore be the implementation of a more versatile optimizer module, that can handle other, possibly more complex, optimization methods and MDO strategies.

It is understood that in the current work not all of the capabilities of the MDO tool developed were explored, given the wide range of possibilities. From the case studies presented, and given that the individual modules were validated (though some issues with the static deformation remain regarding the structural module), it has been observed that this tool is flexible enough to allow single and multidisciplinary wing optimization with substantial improvements over the baseline designs. One important aspect is that the resulting optimized design, especially in terms of internal structure, directly represents a realistic final wing design, rather than simplified structural elements. This is an advantage for an industry where purely academic results are of little consequence.

Also, the interface/framework developed should be understood as an open architecture, since they are intended to serve as a docking point for other, possibly more capable, versions of the analyzer modules here presented. Additionally, other modules may be added in the future (provisions have been made for the inclusion of a cost estimation module, for instance). Extensions to the current modules could, for instance, consist of the extension of the flight envelope of the aerodynamics module into the supersonic regime, along with the capability of analyzing more complex planforms and maneuver conditions. With regard to the structural module, one of the major downsides that has been recognized is the lack of knowledge of the state of stress of the wing structure. To solve this, a higher fidelity methodology must be employed, such as resorting to a dedicated finite element model of the wing. These higher fidelity solutions may require additional computational power, though, especially if the sensitivities are to be computed in a classical fashion.

On a final note, the graphical user interface has proved its usefulness, as it not only makes it easier to formulate the optimization problems, but also to analyze and debug the results, leading to a reformulation of the constraints, for instance.

# References

[1] Antoine, Nicolas E. and Kroo, Ilan M., *Framework for Aircraft Conceptual Design and Environmental Performance Studies*, Vol. 43, No. 10, pp. 2100-2109, October 2005.

[2] Antoine, Nicolas E., Kroo, Ilan M. , *Aircraft Optimization for Minimal Environmental Impact*, Journal of Aircraft, vol.41, No.4, pp. 790-797, August 2004.

[3] R.J. Balling and J. Sobieszczanski-Sobieski, *Optimization of Coupled Systems - A Critical Overview of Aproaches*, NASA Contractor Report 1950519, ICASE Report No. 94-100, NASA Langley Research Center, December 1994.

[4] Kroo, I., Altus, S., Braun, R., Gage, P. and Sobiesky, I., *Multidisciplinary Optimization Methods for Aircraft Preliminary Design*, AIAA 94-4325, Fifth AIAA/USAF/NASA/ISSMO Symposium on Multidisciplinary Analysis and Optimization, Panama City, Florida, $7^{\text{th}}$-$9^{\text{th}}$ September, 1994.

[5] Cramer, E. J., Dennis, Jr., J. E., Frank, P. D., Lewis, R. M., Shubin, G. R. *Problem Formulation for Multidisciplinary Optimization*, Center for Research on Parallel Computation Report CRPC-TR93334, Rice University, Houston, TX, 1993.

[6] Martins, Joaquim R. R. A., *A Coupled-Adjoint Method for High-Fidelity Aero-Structural Optimization*, PhD thesis, Stanford University, CA, USA, October 2002.

[7] Jameson, Antony and Kim, Sangho *Reduction of the Adjoint Gradient Formula in the Continuous Limit*, AIAA Journal, vol.41, No.11, pp. 2114-2129, November 2003.

[8] Bieniawski, S., Kroo, I. and Wolpert, D., *Discrete, Continuous, and Constrained Optimization Using Collectives*, AIAA-2004-4580, 10$^{\text{th}}$ AIAA/ISSMO Multidisciplinary Analysis and Optimization Conference, Albany, New York, 30$^{\text{th}}$-31$^{\text{st}}$ August, 2004.

[9] Sobieski, Jaroslaw Sobieszczanski-, Agte, Jeremy S., Sandusky Jr., Robert R., *Bi-Level Integrated System Synthesis(BLISS)*, NASA/TM-1998-208715, Langley Research Center, Hampton, Virginia, August 1998.

[10] Sobieski, Jaroslaw Sobieszczanski-, Emiley, Mark S., Agte, Jeremy S.,Sandusky Jr., Robert R., *Advancement of Bi-level Integrated System Synthesis (BLISS)*, AIAA-2000-421, 38$^{\text{th}}$ Aerospace Sciences Meeting and Exhibit, Reno, NV, 10$^{\text{th}}$-13$^{\text{th}}$ January, 2000.

[11] Wakayama, Sean, *Blended-Wing-Body Optimization Problem Setup*, AIAA-2000-4740, 8$^{\text{th}}$ AIAA/USAF/NASA/ISSMO Symposium on Multidisciplinary Analysis and Optimization, Long Beach, CA, 6$^{\text{th}}$ - 8$^{\text{th}}$ September, 2000.

[12] Ko, Yan-Yee Andy, *The Multidisciplinary Design Optimization of a Distributed Propulsion Blended-Wing-Body Aircraft*, PhD thesis, Virginia Polytechnic Institute, Blacksburg, VA, 14$^{\text{th}}$ April, 2003.

[13] Bhatia M., Ajmera H. C., Abhyankar S. N., Mujumdar P. M., Sudhakar K., *WingOpt - An MDO Tool for Concurrent Aerodynamic Shape and Structural Sizing Optimization of Flexible Aircraft Wings*, International Conference on Modeling, Simulation, Optimization of Multidisciplinary Engineering Systems, September 24-26, 2003, Goa, India.

[14] Sobester,Andreas and Keaney, Andy J., *Multidisciplinary Design Optimization of UAV Airframes*, AIAA 2006-1612, 47$^{\text{th}}$ AIAA/ASME/ASCE/AHS/ASC Structures, Structural Dynamics and Materials Conference, Newport, Rhode Island, 1$^{\text{st}}$ - 4$^{\text{th}}$ May, 2006.

[15] Deremaux, Yann, *Physically-Based, Real-Time Visualization and Constraint Analysis in Multidisciplinary Design Optimization*, MASc Thesis, Massachussets Institute of Technology, Boston, MA, June 2003.

[16] Choi, Seongim, Alonso, Juan J., Kim, Sangho, Kroo, Ilan M., Wintzer, Mathias, *Two-Level Multi-Fidelity Design Optimization Studies for Supersonic Jets*, 43$^{\text{rd}}$ AIAA Aerospace Sciences Meeting and Exhibit, Reno, NV, USA, 10$^{\text{th}}$-13$^{\text{th}}$ January, 2005.

[17] Margason, R. J., S. O. Kjelgaard, W.L. Sellers III, C.E.K. Morris, Jr., K. B. Walkey and E. W. Shields, *Subsonic Panel Methods - A Comparison of Several Production Codes*, AIAA paper 85-0280, presented at AIAA 23$^{\text{rd}}$ Aerospace Sciences Meeting, Reno, Nev., January 1985.

[18] Bertin, John J., *Aerodynamics for Engineers*, Prentice Hall, 4$^{\text{th}}$ Edition, Upper Saddle River, NJ, 2002.

[19] Mason, W.H., *Aerodynamics of 3D Lifting Surfaces through Vortex Lattice Methods - Applied Computational Aerodynamics Text/Notes*, Department of

Aerospace and Ocean Engineering, Virginia Polytechnic Institute and State University, March 1998.

[20] Lamar, John E. and Margason, Richard J., *Vortex Lattice FORTRAN Program for Estimating Subsonic Aerodynamic Characteristics of Complex Planforms*, NASA Technical Note D-6142, Washington D.C., February 1971.

[21] Katz, Joseph and Plotkin, Allen, *Low Speed Aerodynamics - From Wing Theory to Panel Methods*, McGraw-Hill, 1991.

[22] http://www.ae.uiuc.edu/m-selig/ads/coord_database.html, viewed December 2006 and September 2007.

[23] Drela, Mark and Youngren, Harold, *AVL (Athena Vortex Lattice) 3.26 User Primer*, Massachussets Institute of Technology, Boston, MA, April 2006.

[24] Mason, W.H., *Manual for Program FRICTION*, Virginia Tech Aerospace Engineering Aerodynamics and Design Software Collection.

[25] Corke, Thomas C., *Design of Aircraft*, Prentice Hall, Upper Saddle River, NJ, 2002.

[26] McCormick, Barnes W., *Aerodynamics, Aeronautics and Flight Mechanics*, 2nd Edition, John Wiley & Sons, 1995.

[27] Melin, Tomas, *A Vortex Lattice MATLAB Implementation for Linear Aerodynamic Wing Applications*, Royal Institute of Technology (KTH), Department of Aeronautics, December 2000.

[28] Gumbert, Clyde R., Hou, Gene J. -W. and Newman Perry A., *High-Fidelity Computational Optimization for 3-D Flexible Wings: Part I - Simultaneous Aero-*

*Structural Design Optimization (SASDO)*, Journal of Optimization and Engineering, Vol.6, pp. 117-138, 2005.

[29] Chao., D. D. and van Dam, C. P. , *Wing Drag Prediction and Decomposition*, Vol. 43, No. 1, pp. 82-90, JanuaryFebruary 2006.

[30] Kapania, Rakesh K. and Liu, Youhua, *Static and Vibration Analyses of General Wing Structures Using Equivalent-Plate Models*, AIAA Journal, Vol.38, No.7, pp. 1269-1277, July 2000.

[31] Gern, Frank H., Inman, Daniel J. and Kapania, Rakesh K., *Structural and Aeroelastic Modeling of General Planform Wings with Morphing Airfoils*, AIAA Journal, Vol. 40, No. 4, pp. 628-637, April 2002.

[32] Tizzi, Silvano, *Numerical Procedure for the Dynamic Analysis of Three-Dimensional Aeronautical Structures*, Journal of Aircraft, Vol. 34, No. 1, pp. 120-130, JanuaryFebruary 1997.

[33] Gary L. Giles, *Equivalent Plate Analysis of Aircraft Wing Box Structures with General Planform Geometry*, Vol. 23, No. 11, pp. 859-864, November 1986.

[34] Livne, Eli, *Equivalent Plate Structural Modeling for Wing Shape Optimization Including Transverse Shear*, AIAA Journal, Vol. 32, No. 6, pp. 1278-1288, June 1994.

[35] Livne, Eli and Navarro, Israel, *Nonlinear Equivalent Plate Modeling of Wing-Box Structures*, Journal of Aircraft, Vol. 36, No. 5, pp. 851-865, SeptemberOctober 1999.

[36] Ghugal, Y. M. and Shimpi, R. P., *A Review of Refined Shear Deformation Theories of Isotropic and Anisotropic Laminated Plates*, Journal of Reinforced Plastics and Composites, Vol. 21, No. 9, pp. 775-813, 2002.

[37] Gabriel, Rui, *Development of Equivalent Plate Models for Aircraft Wing Structures*, MASc thesis, Instituto Superior Tecnico, Lisbon, Portugal, October 2007.

[38] Megson, T. H. G., *Aircraft Structures for Engineering Students - $2^{nd}$ edition*, Edward Arnold, pp. 521-557, 1990.

[39] Theodorsen, Theodore and Garrick, I. E., *Mechanism of Flutter - A Theoretical and Experimental Investigation of the Flutter Problem*, NACA Report No. 685, 1940.

[40] Martin, Dennis J., *Summary of Flutter Experiences as a Guide to the Preliminary Design of Lifting Surfaces on Missiles*, NACA TN 4197, Langley Aeronautical Laboratory, Langley Field, VA, February 1958.

[41] Arora, Jasbir S., *Introduction to Optimum Design*, McGraw Hill, 1989.

[42] Kroo, Ilan M., *Nonplanar Wing Concepts for Increased Aircraft Efficiency*, VKI lecture series on Innovative Configurations and Advanced Concepts for Future Civil Aircraft, $6^{th}$ - $10^{th}$ June, 2005.

[43] Gonzalez, Luis F. et al., *Multidisciplinary Optimization of Unmanned Aerial Vehicles (UAV) using Multi-Criteria Evolutionary Algorithms*, $6^{th}$ World Congress of Structural and Multidisciplinary Optimization, Rio de Janeiro, Brazil, $30^{th}$ May - $3^{rd}$ June, 2005.

[44] Crawford, Curran A., *Advanced Engineering Models for Wind Turbines with Application to the Design of a Coning Rotor Concept*, PhD thesis, University of Cambridge, 2006.

[45] Korte, J. J., Salas, A. O., Dunn, H. J., Alexandrov, N. M., Follett, W. W., Orient, G. E. and Hadid, A. H. *Multidisciplinary Approach to Linear Aerospike Nozzle*

*Optimization*, AIAA-1997-3374, 33rd AIAA/ASME/SAE/ASEE Joint Propulsion Conference and Exhibit, Seattle, WA, 6th-9th July, 1997.

[46] Martins, Joaquim R. R. A., Alonso, Juan J. and Reuther, James J., *Complete Configuration Aero-Structural Optimization Using a Coupled Sensitivity Analysis Method*, AIAA 20025402, 9th AIAA/ISSMO Symposium on Multidisciplinary Analysis and Optimization, Atlanta, GA, 4th 6th September, 2002.

[47] Manolache, Florin B. and Costiner, Sorin *Parallel Processing Approaches for Multi Disciplinary Optimization Algorithms*, CNA Scientific Report 02-CNA-009, 2002.

[48] http://www.boeing.com/commercial/787family/specs.html, viewed September 2007.

[49] http://www.lissys.demon.co.uk, viewed September 2007.

[50] http://adg.stanford.edu/aa241/AircraftDesign.html, viewed December 2006 and June 2007.

# Appendix A

# The horseshoe vortex

As a solution of the Laplace equation, the velocity field due to the presence of a vortex is defined in polar coordinates as (point vortex located at the origin of the coordinate system):

$$\mathbf{V} = \frac{\Gamma}{2\pi r}\mathbf{e}_\theta \tag{A.1}$$

Expanding this definition into the three dimensional realm [19] (Figure A.1):

$$d\mathbf{V} = \frac{\Gamma}{4\pi}\frac{d\mathbf{l} \times \mathbf{r_{QP}}}{|\mathbf{r_{QP}}|^3} \tag{A.2}$$

In order to obtain the velocity induced by a finite length of vortex filament at point P, Eq. (A.2) is integrated:

$$\mathbf{V} = \frac{\Gamma}{4\pi}\int \frac{d\mathbf{l} \times \mathbf{r_{QP}}}{|\mathbf{r_{QP}}|^3} \tag{A.3}$$

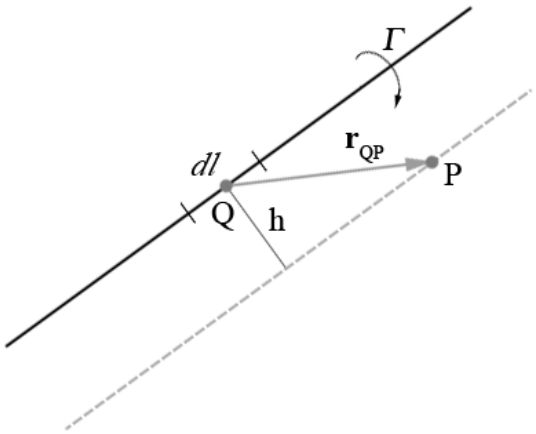


Figure A.1: Straight vortex filament [19]

Since $\mathbf{V}$ is orthogonal to both $d\mathbf{l}$ and $\mathbf{r_{QP}}$:

$$d\mathbf{l} \times \mathbf{r_{QP}} = |d\mathbf{l}|\,|\mathbf{r_{QP}}| \sin\theta \, \frac{\mathbf{V}}{|\mathbf{V}|} \tag{A.4}$$

$\theta$ being the angle between $\mathbf{r_{QP}}$ and $d\mathbf{l}$ (Figure A.2).

So that Eq. (A.2) may be rewritten as:

$$d\mathbf{V} = \frac{\Gamma}{4\pi} \frac{\mathbf{V}}{|\mathbf{V}|} \sin\theta \, \frac{|d\mathbf{l}|}{|\mathbf{r_{QP}}|^2} \tag{A.5}$$

From inspection of Figure A.1:

$$|d\mathbf{l}| = h \csc^2\theta d\theta \tag{A.6}$$

$$|\mathbf{r_{QP}}| = \frac{h}{\sin\theta} \tag{A.7}$$

Combining these with Eq. (A.5) and then proceeding with the integration as in

Eq. (A.3):

$$|\mathbf{V}| = \frac{\Gamma}{4\pi h} \int_{\theta=\theta_1}^{\theta=\theta_2} \sin\theta \; d\theta \tag{A.8}$$

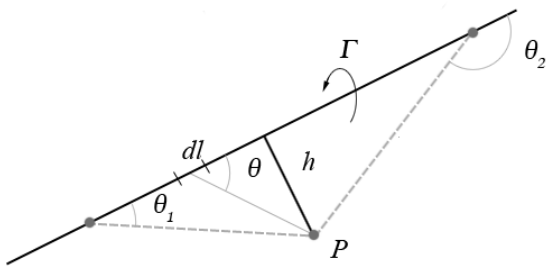


Figure A.2: Angles $\theta_1$ and $\theta_2$ [19]

Eq. (A.8) now allows the evaluation of the magnitude of the induced velocity due to any type of straight vortex filament (the direction of the induced velocity is set, of course, by the cross product between $d\mathbf{l}$ and $\mathbf{r_{QP}}$). In the classical vortex lattice method, two important cases arise: the finite vortex and the semi-infinite vortex.

$$|\mathbf{V}| = \frac{\Gamma}{4\pi h} (\cos\theta_1 - \cos\theta_2) \tag{A.9}$$

$$|\mathbf{V}| = \frac{\Gamma}{4\pi h} (1 + \cos\theta_1) \tag{A.10}$$

Now we may start constructing expressions for the velocity induced by a horseshoe vortex element, which, as already mentioned in Chapter 2 is composed of one (bound) finite vortex filament and two (trailing) semi infinite vortices. It is the useful to relate the aforementioned angles with the distances between points of interest. From Figure A.3 we extract the following:

$$h = r_P = \frac{|\mathbf{r}_1 \times \mathbf{r}_2|}{|\mathbf{r}_0|} \tag{A.11}$$

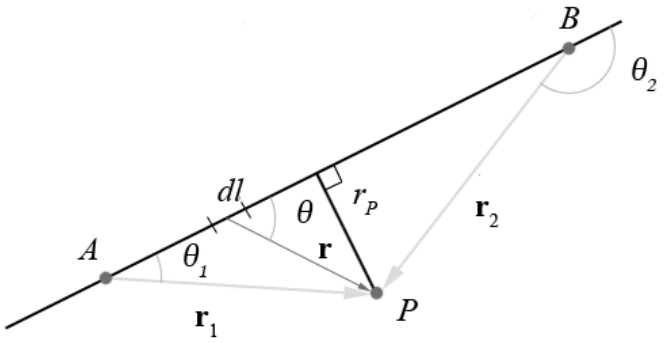


Figure A.3: Nomenclature for the straight vortex filament [19]

$$\cos\theta_1 = \frac{\mathbf{r}_0 \cdot \mathbf{r}_1}{|\mathbf{r}_0|\,|\mathbf{r}_1|} \tag{A.12}$$

$$\cos\theta_2 = \frac{\mathbf{r}_0 \cdot \mathbf{r}_2}{|\mathbf{r}_0|\,|\mathbf{r}_2|} \tag{A.13}$$

So that:

$$\mathbf{V} = \frac{\Gamma}{4\pi}\frac{|\mathbf{r}_0|}{|\mathbf{r}_1 \times \mathbf{r}_2|}\left(\frac{\mathbf{r}_0 \cdot \mathbf{r}_1}{|\mathbf{r}_0|\,|\mathbf{r}_1|} - \frac{\mathbf{r}_0 \cdot \mathbf{r}_2}{|\mathbf{r}_0|\,|\mathbf{r}_2|}\right)\frac{\mathbf{r}_1 \times \mathbf{r}_2}{|\mathbf{r}_1 \times \mathbf{r}_2|} = \frac{\Gamma}{4\pi}\frac{\mathbf{r}_1 \times \mathbf{r}_2}{|\mathbf{r}_1 \times \mathbf{r}_2|^2}\left[\mathbf{r}_0 \cdot \left(\frac{\mathbf{r}_1}{|\mathbf{r}_1|} - \frac{\mathbf{r}_2}{|\mathbf{r}_2|}\right)\right] \tag{A.14}$$

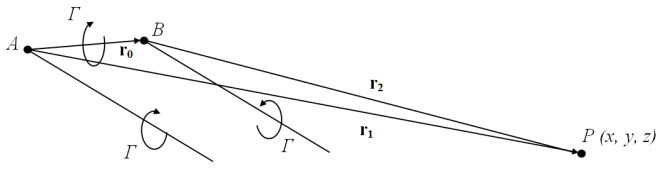


Figure A.4: Horseshoe vortex

We may now superimpose the contributions from the three different filaments that form a horseshoe vortex (see Figure A.4) in order to obtain the final expression for the induced velocity at an arbitrary point. From the above, and using $A\,(x_{1n}, y_{1n}, z_{1n})$,

$B\left(x_{2n}, y_{2n}, z_{2n}\right)$ and $P\left(x, y, z\right)$:

$$\mathbf{V_{AB}} = \frac{\Gamma}{4\pi}\left\{Fac1_{AB}\right\}\ \left\{Fac2_{AB}\right\} \tag{A.15}$$

$$\begin{aligned}\left\{Fac1_{AB}\right\} = \frac{}{}&\left\{\left[\left(y-y_{1n}\right)\left(z-z_{2n}\right)-\left(y-y_{2n}\right)\left(z-z_{1n}\right)\right]\mathbf{i}\right.\\&-\left[\left(x-x_{1n}\right)\left(z-z_{2n}\right)-\left(x-x_{2n}\right)\left(z-z_{1n}\right)\right]\mathbf{j}\\&\left.+\left[\left(x-x_{1n}\right)\left(y-y_{2n}\right)-\left(x-x_{2n}\right)\left(y-y_{1n}\right)\right]\mathbf{k}\right\}\\&\overline{\left\{\left[\left(y-y_{1n}\right)\left(z-z_{2n}\right)-\left(y-y_{2n}\right)\left(z-z_{1n}\right)\right]^2\right.}\\&+\left[\left(x-x_{1n}\right)\left(z-z_{2n}\right)-\left(x-x_{2n}\right)\left(z-z_{1n}\right)\right]^2\\&\left.+\left[\left(x-x_{1n}\right)\left(y-y_{2n}\right)-\left(x-x_{2n}\right)\left(y-y_{1n}\right)\right]^2\right\}\end{aligned} \tag{A.16}$$

$$\begin{aligned}\left\{Fac2_{AB}\right\} = {}&\frac{\left(x_{2n}-x_{1n}\right)\left(x-x_{1n}\right)+\left(y_{2n}-y_{1n}\right)\left(y-y_{1n}\right)+\left(z_{2n}-z_{1n}\right)\left(z-z_{1n}\right)}{\sqrt{\left(x-x_{1n}\right)^2+\left(y-y_{1n}\right)^2+\left(z-z_{1n}\right)^2}}-\\&\frac{\left(x_{2n}-x_{1n}\right)\left(x-x_{2n}\right)+\left(y_{2n}-y_{1n}\right)\left(y-y_{2n}\right)+\left(z_{2n}-z_{1n}\right)\left(z-z_{2n}\right)}{\sqrt{\left(x-x_{2n}\right)^2+\left(y-y_{2n}\right)^2+\left(z-z_{2n}\right)^2}}\end{aligned} \tag{A.17}$$

$$\mathbf{V_{A\infty}} = \frac{\Gamma_n}{4\pi}\left\{\frac{\left(z-z_{1n}\right)\mathbf{j}+\left(y_{1n}-y\right)\mathbf{k}}{\left(z-z_{1n}\right)^2+\left(y_{1n}-y\right)^2}\right\}\left[1.0+\frac{x-x_{1n}}{\sqrt{\left(x-x_{1n}\right)^2+\left(y-y_{1n}\right)^2+\left(z-z_{1n}\right)^2}}\right] \tag{A.18}$$

$$\mathbf{V_{B\infty}} = \frac{\Gamma_n}{4\pi}\left\{\frac{\left(z-z_{2n}\right)\mathbf{j}+\left(y_{2n}-y\right)\mathbf{k}}{\left(z-z_{2n}\right)^2+\left(y_{2n}-y\right)^2}\right\}\left[1.0+\frac{x-x_{2n}}{\sqrt{\left(x-x_{2n}\right)^2+\left(y-y_{2n}\right)^2+\left(z-z_{2n}\right)^2}}\right] \tag{A.19}$$

The total induced velocity will then be:

$$\mathbf{V}_{ind} = \mathbf{V_{AB}} + \mathbf{V_{A\infty}} + \mathbf{V_{B\infty}} \tag{A.20}$$

# Appendix B

# Skin friction and form drag calculation

The method as described in [19], uses the *Eckert Reference Temperature* method for laminar flow and the *van Driest II formula* for turbulent flow to compute skin friction. For each of these, some assumptions are made, the most relevant of which being that $\frac{T_w}{T_{aw}} = 1$, i.e., the surface (wall) temperature is such that it is equal to the adiabatic wall temperature (hence, no heat transfer). The form factor ($FF$) to be used in Eq. (2.8) is taken from [25]. All air data ($T$, $\rho$) is computed from user supplied information of the flight altitude and is based on the International Standard Atmosphere (ISA) charts.

In the current approach, the wing is divided into spanwise strips. At each of those, the values of the chord ($c\,(y)$), maximum thickness to chord ratio ($\left(\left(\frac{t}{c}\right)_{\max}(y)\right)$) and chordwise location of the maximum thickness to chord ratio ($\left(\left(\frac{x}{c}\right)_{\left(\frac{t}{c}\right)_{\max}}(y)\right)$). A local $Re$ is then computed:

$$Re_L = \frac{\rho V_\infty \cos\left(\Lambda_{LE}\right) c\,(y)}{\mu} \tag{B.1}$$

in which the dynamic viscosity ($\mu$), is computed according to Sutherland's law:

$$\mu = 1.458 \times 10^{-6} \sqrt{\frac{T}{1 + 110.4T}} \tag{B.2}$$

Based on the supplied $Re_{trans}$ (see footnote in Sec. 2.3), the chordwise location of the laminar-turbulent boundary layer transition is calculated as:

$$\frac{x_{trans}}{c} = \frac{Re_{trans}}{Re_L} \tag{B.3}$$

in case that $Re_{trans} > Re_L$ then $Re_{trans} = Re_L$.

In order to compute the laminar friction coefficient $C_{f_{lam}}$, the following values are assumed for compressible flow: $\gamma = 1.4$, $Pr = 0.72$, $r = \sqrt{Pr} = \sqrt{0.72}$ and the edge temperature, $T_e = T$. The procedure for a given value of $Re$ is then:

$$\frac{T_w}{T_e} = \frac{T_w}{T_{aw}} \left( \frac{1 + r\,(\gamma - 1)\,M^2}{2} \right) \tag{B.4}$$

$$\frac{T^*}{T_e} = 0.5 + 0.039M^2 + 0.5\frac{T_w}{T_e} \tag{B.5}$$

$$C^* = \sqrt{\frac{T^*}{T_e}} \left( \frac{1 + \frac{T_k}{T_e}}{\frac{T^*}{T_e} + \frac{T_k}{T_e}} \right) \tag{B.6}$$

So that:

$$C_{f_{lam}} = 0.664 \sqrt{\frac{C^*}{Re}} \tag{B.7}$$

For the turbulent friction coefficient: $\gamma = 1.4$, $r = 0.88$ and again $T_e = T$.

$$x_m = (\gamma - 1)\,\frac{M^2}{2} \tag{B.8}$$

$$F = \frac{T_w}{T_e} = \frac{T_w}{T_{aw}} \frac{T_{aw}}{T_e} \tag{B.9}$$

$$\frac{T_{aw}}{T_e} = 1 + r\,x_m \tag{B.10}$$

$$T_w = F\,T_e \tag{B.11}$$

$$A = \sqrt{\frac{r\,x_m}{F}} \tag{B.12}$$

$$B = \frac{1 + r\,x_m - F}{F} \tag{B.13}$$

$$\alpha = \frac{2A^2 - B}{(4A^2 + B^2)^{\frac{1}{2}}} \tag{B.14}$$

$$\beta = \frac{B}{(4A^2 + B^2)^{\frac{1}{2}}} \tag{B.15}$$

$$F_c = \begin{cases} \frac{r\,x_m}{(\csc(\alpha)+\csc(\beta))^2}, & M_\infty > 0.1 \\ \left(\frac{1+\sqrt{F}}{2}\right)^2, & M_\infty \leq 0.1 \end{cases} \tag{B.16}$$

$$F_\theta = \frac{\mu_e}{\mu_w} = \sqrt{\frac{1}{F}} \left( \frac{1 + \frac{122}{T_w} \times 10^{-\frac{5}{T_w}}}{1 + \frac{122}{T_e} \times 10^{-\frac{5}{T_e}}} \right) \tag{B.17}$$

$$F_x = \frac{F_\theta}{F_C} \tag{B.18}$$

For a specified value of $Re$ we define:

$$\overline{Re} = F_x\ Re \tag{B.19}$$

$$\frac{0.242}{\sqrt{\overline{C_f}}} = \log_{10}\left(\overline{Re}\ \overline{C_f}\right) \tag{B.20}$$

To solve Eq. B.20, the Newton method is employed:

$$C_f\,(initial\ guess) = \frac{0.074}{\left(\overline{Re}\right)^{0.2}} \tag{B.21}$$

$$\left(\overline{C_f}\right)^{i+1} = \left(\overline{C_f}\right)^{i} \left( 1 + \frac{0.242 - \sqrt{\left(\overline{C_f}\right)^{i}} \log_{10}\left(Re\left(\overline{C_f}\right)^{i}\right)}{0.121 + \frac{\sqrt{\left(\overline{C_f}\right)^{i}}}{\log(10)}} \right) \tag{B.22}$$

$$C_{f_{turb}} = \frac{\overline{C_f}}{F_c} \tag{B.23}$$

Using Eqs. B.7 and B.23 we can compute ($N$ is the spanwise number of strips):

$$C_{D_f} = \sum_{i=1}^{N} FF \frac{S_{wet}}{S_{ref}} \left( C_{f_{turb}}\left(Re_L\right) - \frac{x_{trans}}{c}\left(C_{f_{turb}}\left(Re_{trans}\right) - C_{f_{lam}}\left(Re_{trans}\right)\right)\right) \tag{B.24}$$

Where the form factor is [25] (for each strip):

$$FF = 1 + \frac{0.6}{\frac{\left(\frac{x}{c}\right)}{\left(\frac{t}{c}\right)_{\max}}} \left(\frac{t}{c}\right)_{\max} + 100 \left( \left(\frac{t}{c}\right)_{\max} \right)^4 \tag{B.25}$$

And the wetted area, $S_{wet}$ is defined as:

$$S_{wet} = \begin{cases} \frac{2.003\, S_{ref}}{\cos\varphi} & \left(\frac{t}{c}\right)_{\max} < 0.05 \\ \left(1.977 + 0.52\frac{t}{c}\right)\frac{S_{ref}}{\cos\varphi} & \left(\frac{t}{c}\right)_{\max} \geq 0.05 \end{cases} \tag{B.26}$$

# Appendix C

# Material properties

## C.1 Aluminum

Table C.1: Material properties for aluminum

| **Property** | **Value** |
|---|---|
| Young's Modulus, $E$ | 70 GPa |
| Shear Modulus, $G$ | 20 GPa |
| Poisson ratio, $\nu$ | 0.33 |
| Density | 2700 Kg.m$^{-3}$ |

## C.2 Carbon fiber composite

Table C.2: Material properties for carbon fiber composite skin

| **Property** | **Value** |
|---|---|
| Young's Modulus, $E_X$ | 230 GPa |
| Young's Modulus, $E_Y$ | 230 GPa |
| Shear Modulus, $G_{XY}$ | 20 GPa |
| Shear Modulus, $G_{XZ}$ | 10 GPa |
| Shear Modulus, $G_{YZ}$ | 10 GPa |
| Poisson ratio, $\nu_{xy}$ | 0.30 |
| Poisson ratio, $\nu_{yx}$ | 0.30 |
| Density | 1800 Kg.m$^{-3}$ |